GR Focus

CHIME dating of monazite, xenotime, zircon and polycrase: Protocol, pitfalls and chemical criterion of possibly discordant age data

Kazuhiro Suzuki *, Takenori Kato

The Center for Chronological Research, Nagoya University, Chikusa-ku, Nagoya 464-8602, Japan

Abstract

This paper outlines the CHIME (chemical Th–U-total Pb isochron method) dating method, which is based on precise electron microprobe analyses of Th, U and Pb in Th- and U-bearing accessory minerals such as monazite, xenotime, zircon and polycrase. The age-mapping technique that is applicable to young monazite and zircon is also described. CHIME dating consists of analyzing multiple spots within homogeneous age domains that show sufficient compositional variation, and then these data are used to construct a "pseudo-isochron" from which an age can be obtained via regression. This method, when coupled with discrimination of possibly concordant age data by chemical criteria such as the $(Ca+Si)/(Th+U+Pb+S)$ ratio for monazite and Ca and S contents for zircon, has the potential advantage of significant precision, and the ability to work with minerals that have a significant initial common Pb component. This technique can identify two or more homogeneous domains that are separated by age gaps smaller than the error on individual spot age analysis. Many features that are insignificant in major element analysis can have major impact in the acquisition of trace element data. Critical factors include the roles of collimator slit, detector gas, background estimation, accelerating voltage, probe current, X-ray interferences and count rate in affecting the accuracy, and a way to apply the Th and U interference correction without pure Th- and U-oxides or synthesized pure $ThSiO_4$. The age-mapping procedure for young monazite and zircon includes acquiring $PbM\alpha$ (or $PbM\beta$) intensity of individual pixels with multiple spectrometers, correcting background with background maps computed from a measured background intensity by the intensity relationships determined in advance of the measurement, calibrating of intensity with standards and calculating of ages from the Th, U and Pb concentrations. This technique provides age maps that show differences in age domains on the order of 20 Ma with in monazite as young as 100 Ma. The effect of sample damage by irradiation of intense and prolonged probe measurement is also described.
© 2008 International Association for Gondwana Research. Published by Elsevier B.V. All rights reserved.

Contents

---

* Corresponding author. Tel.: +81 52 789 3090; fax: +81 52 789 3090.
  E-mail address: suzuki@nendai.nagoya-u.ac.jp (K. Suzuki).

1. Introduction

Chemical dating using the electron probe microanalyzer (EPMA) has become increasingly popular since the proposal of the CHIME method which was a novel approach for micron-scale dating of monazite, zircon and other Th- and U-bearing accessory minerals (Suzuki et al., 1991; Suzuki and Adachi, 1991a,b). Prior to the CHIME method, chemical mineral dating on EPMA had been carried out by Cameron-Schimann (1978), Parslow et al. (1985), Lumpkin and Chakoumakos (1988) and Bowles (1990). These pioneers had used uraninite, huttonite and thorite as a target, because these minerals yield large amounts of Pb during a given time span. Uraninite, huttonite and thorite, however, are likely to be metamict, and show discordant relationships in the Th–U–Pb system. Since the EPMA measures element concentrations rather than isotopes, it is important that the analyzed domain has remained closed after formation and as such the isotopic data yields concordant ages.

Monazite gives essentially concordant U–Pb and Th–Pb ages (e.g. Burger et al., 1965; Köppel and Grünenfelder, 1971; Grauert et al., 1974; Köppel, 1974), and contains little initial Pb compared with radiogenic Pb (Williams et al., 1983; Corfu, 1988). The concordance in Th–Pb and U–Pb systems has also been noted in xenotime (Hawkins and Bowring, 1997). Zircon, on the other hand, often shows a discordant U–Pb relationship (Tilton et al., 1957; Silver and Deutsch, 1963). Williams et al. (1984) revealed a reverse discordance: the concentration of radiogenic Pb is higher than what can be generated by radioactive decay of coexisting U and Th. The discordance is explained in terms of Pb-loss and gain owing to the migration of gaseous daughters (Rn) through radiation damage (Suzuki, 1987a). Schärer and Allègre (1982), however, showed by the fragment analysis that micron-scale domains within a single zircon can remain as a closed system. Th- and U-rich accessory minerals, at least in microdomains, can remain as a closed system, and are feasible to be dated chemically with EPMA.

Most EPMA dating studies utilize monazite (e.g., Suzuki et al., 1991; Suzuki and Adachi, 1991a,b; Montel et al., 1996; Cocherie et al., 1998; Williams et al., 1999, Williams and Jercinovic, 2002; Pyle et al., 2005b; Santosh et al., 2003). This technique has been also applied to zircon and xenotime (Suzuki and Adachi, 1991a,b; Geisler and Schleicher, 2000; Asami et al., 2002, 2005; Biju-Sekhar et al., 2003; Hokada et al., 2004; Santosh et al., 2003), and baddeleyte (French et al., 2002). Xenotime and allanite potentially dissolve Pb-bearing end-members, wakefieldite-Ce ((Ce,Pb)VO₄, originally named as kusuite; Deliens and Piret, 1977) and hancockite ((Ca,Pb,Sr)₂ (Al,Fe³⁺)₃(SiO₄)(Si₂O₇)(OH); Dunn, 1985). The amount of

these components, however, is negligibly small under favorable circumstances. Although euxenite–polycrase and allanite tend to show discordant Th–U–Pb relations, some give reliable age information (Suzuki et al., 2006). Thus the EPMA dating technique is now commonly applied to the wide spectra of geological examples. Articles that use the dating technique are published by many scientific journals including Gondwana Research (Nishiya et al., 2003; Santosh et al., 2003, 2004, 2005, 2006a,b,c, 2007; Suzuki et al., 2006; Souza et al., 2006; Upadhyay et al., 2006; Dunkley et al., 2008-this issue; Kusiak et al., 2008-this issue; Tetsopgang et al., 2008-this issue).

In this paper, we summarize the critical components of EPMA chemical dating: (1) the basis of CHIME age calculation method, (2) hardware configuration including accelerating voltage, beam current, background measurement and correction of elemental interferences, and (3) protocols for spot by spot analysis and age mapping. Several other considerations will be briefly discussed for proper understanding of the appropriate limitations and the potentials of chemical dating to decipher chronological aspects of geological processes.

2. CHIME age calculation

Each EPMA chemical dating method is based on the bulk parent–daughter relation in the Th–U–Pb system. Natural Th consists mainly of a radioactive nuclide of ^{232}Th and natural U consists mainly of two radioactive nuclides, ^{235}U and ^{238}U. These nuclides decay into Pb:

$$^{232}\text{Th} \rightarrow 6 \text{ alphas} + 4 \text{ betas} + {}^{208}\text{Pb} \tag{1a}$$

$$^{235}\text{U} \rightarrow 7 \text{ alphas} + 4 \text{ betas} + {}^{207}\text{Pb} \tag{1b}$$

$$^{238}\text{U} \rightarrow 8 \text{ alphas} + 6 \text{ betas} + {}^{206}\text{Pb}. \tag{1c}$$

The number of atoms of ^{208}Pb, ^{207}Pb and ^{206}Pb which accumulate in a time t is given in terms of the present-day number of ^{232}Th, ^{235}U and ^{238}U.

$$^{208}\text{Pb} = {}^{232}\text{Th} \{\exp(\lambda_{232}t) - 1\} \tag{2a}$$

$$^{207}\text{Pb} = {}^{235}\text{U} \{\exp(\lambda_{235}t) - 1\} \tag{2b}$$

$$^{206}\text{Pb} = {}^{238}\text{U} \{\exp(\lambda_{238}t) - 1\} \tag{2c}$$

where λ symbolizes the decay constant of each nuclide; $\lambda_{232} = 4.9475 \times 10^{-11}$ y^{-1}, $\lambda_{235} = 9.8485 \times 10^{-10}$ y^{-1} and $\lambda_{238} = 1.55125 \times 10^{-10}$ y^{-1} (Steiger and Jäger, 1977). Thorium- and uranium-bearing minerals contain initial Pb as well as radiogenic:

$$
\begin{aligned}
\text{Total Pb} &= \text{Pb}_{\text{initial}} + {}^{208}\text{Pb} + {}^{207}\text{Pb} + {}^{206}\text{Pb} \\
&= \text{Pb}_{\text{initial}} + {}^{232}\text{Th}\{\exp(\lambda_{232}t) - 1\} \\
&\quad + {}^{235}\text{U}\{\exp(\lambda_{235}t) - 1\} \\
&\quad + {}^{238}\text{U}\{\exp(\lambda_{238}t) - 1\}
\end{aligned}
\tag{3}
$$

Because the ${}^{238}\text{U}/{}^{235}\text{U}$ ratio is 137.88 (Steiger and Jäger, 1977), Suzuki and Adachi (1991a,b) converted the above equation into:

$$
\begin{aligned}
\text{Total Pb} = \text{Pb}_{\text{initial}} &+ \text{Th}\{\exp(\lambda_{232}t) - 1\} \\
&+ \text{U}[\{\exp(\lambda_{235}t) + 137.88\exp(\lambda_{238}t)\}/138.88 - 1].
\end{aligned}
\tag{4}
$$

If initial Pb is assumed to be zero, we can calculate the age from a single set of Th, U and Pb concentrations. This assumption, however, is not self-evident.

The CHIME procedure is as follows. We obtain first an apparent age (t) from each set of the ThO_2, UO_2 and PbO determinations (wt.%) by solving the age equation:

$$
\begin{aligned}
\text{PbO}/W_{\text{Pb}} = (\text{ThO}_2/W_{\text{Th}}) &\times \{\exp(\lambda_{232}t) - 1\} \\
&+ (\text{UO}_2/W_{\text{U}}) \times [\{\exp(\lambda_{235}t) \\
&+ 137.88\exp(\lambda_{238}t)\}/138.88 - 1]
\end{aligned}
\tag{5}
$$

where W symbolizes the gram-molecular weight of each oxides; $W_{\text{Th}} = 264$ (232 + 32), $W_{\text{U}} = 270$ (238 + 32), $W_{\text{Pb}} = 224$ (208 + 16) for Th-rich minerals and $W_{\text{Pb}} = 222$ (206 + 16) for U-rich minerals. Taking the apparent age, we convert the sum of measured ThO_2 and UO_2 into ThO_2^* (Th-rich minerals) or UO_2^* (U-rich minerals) by

$$
\begin{aligned}
\text{ThO}_2^* = \text{ThO}_2 + \text{UO}_2(W_{\text{Th}}/W_{\text{U}}) &\times [\{\exp(\lambda_{235}t) \\
&+ 137.88\exp(\lambda_{238}t)\}/138.88 - 1]/\{\exp(\lambda_{232}t) - 1\}
\end{aligned}
\tag{6a}
$$

$$
\begin{aligned}
\text{UO}_2^* &= \text{UO}_2 + 138.88\text{ThO}_2 \times W_{\text{U}}\{\exp(\lambda_{232}t) - 1\}/\text{UO}_2^* \\
&= \text{UO}_2 + 138.88\text{ThO}_2 \times W_{\text{U}}\{\exp(\lambda_{232}t) - 1\} \\
&\quad /[W_{\text{Th}} \times \{137.88\exp(\lambda_{238}t) + \exp(\lambda_{235}t) - 138.88\}].
\end{aligned}
\tag{6b}
$$

Mineral grains show a variation in Th and U concentrations within domains of a single generation as is demonstrated by sector zoning. Domains of a single generation within individual grains may be identified by means of optical microscope, back-scattered electron (BSE) image, cathode luminescence image and elemental mapping. If domains and/or mineral grains of a single generation have the same amounts of initial Pb but different amounts of Th and U, and have remained in a closed system, all analytical data will lie on a straight line with the slope

(m) and intercept (b):

$$
\text{PbO} = m \times \text{ThO}_2^* + b \qquad \text{(Th-rich mineral)}
\tag{7a}
$$

$$
\text{PbO} = m \times \text{UO}_2^* + b \qquad \text{(U-rich mineral)}.
\tag{7b}
$$

We determine the best-fitting regression line through the procedure proposed by York (1966), taking account of uncertainties in the microprobe analysis, and calculate the first estimation of age (T) from the slope (m) of equations:

$$
T = \ln\{m(W_{\text{Th}}/W_{\text{Pb}}) + 1\}/\lambda_{232} \qquad \text{(Th-rich mineral)}
\tag{8a}
$$

$$
\begin{aligned}
m(W_{\text{U}}/W_{\text{Pb}}) &= \{\exp(\lambda_{235}T) + 137.88 \exp(\lambda_{238}T)\} \\
&\quad /138.88 - 1 \qquad \text{(U-rich mineral)}.
\end{aligned}
\tag{8b}
$$

Then, we can obtain the improved estimation by replacing the apparent ages (t) with the first age estimate (T), and by iterating the operation. The intercept (b) of the line is assumed to represent the concentration (in wt.%) of the initial PbO of all data points. A sufficient amount of initial Pb or Pb-loss, if present, would deviate the line from the origin, or result in scattering of data points. The statistical measure of the goodness of fit of data to a line is given by mean square of weighted deviation (MSWD):

$$
\text{MSWD} = \frac{(Y_i - mX_i - b)^2/(y_i + m^2x_i)}{(n-2)}
\tag{9}
$$

where x_i and y_i represent variances of individual data point (X_i, Y_i), m and b the slope and intercept of a fitted line and n the number of data points. The MSWD decreases with improving fit, but can become unacceptably low if the analytical errors in the microprobe analyses are overestimated. Readers can calculate the CHIME age and MSWD using the CHIME age calculation program (e.g., Kato et al., 1999: http://www.nendai.nagoya-u.ac.jp/gsd/CHIME/).

As initial Pb in monazite is always low (Parrish, 1990), Montel et al. (1996) proposed the calculation of monazite age from the age Eq. (4) by assuming no initial Pb, and estimation of a probable age from several determinations after propagating uncertainties with a representation by a bell-shaped probability curve. This graphical representation allows, to some extent, the visualization of whether or not the population of age data is consistent with a single geological event, unambiguously defines two successive events, or is too broadly dispersed or just shows a few outliers. Rhede et al. (1996) represented the age equation (3) for monazite by an equation of a plane in three-dimensional ThO_2–UO_2–PbO space:

$$
\text{PbO} = a\text{ThO}_2 + b + c\text{UO}_2
\tag{10}
$$

with $a = (1/W_{\text{Th}}) \times [\exp(\lambda_{232}t) - 1]$ and $c = (1/W_{\text{U}}) \times [\{\exp(\lambda_{235}t) + 138\exp(\lambda_{238}t)\}/139 - 1]$. The parameters a, b and c are estimated through error-weighted least-square regression, and then the U/Pb and Th/Pb ages are determined independently of the estimated parameters. The parameter b represents the average initial Pb of all data points. Because initial Pb in monazite is assumed to be
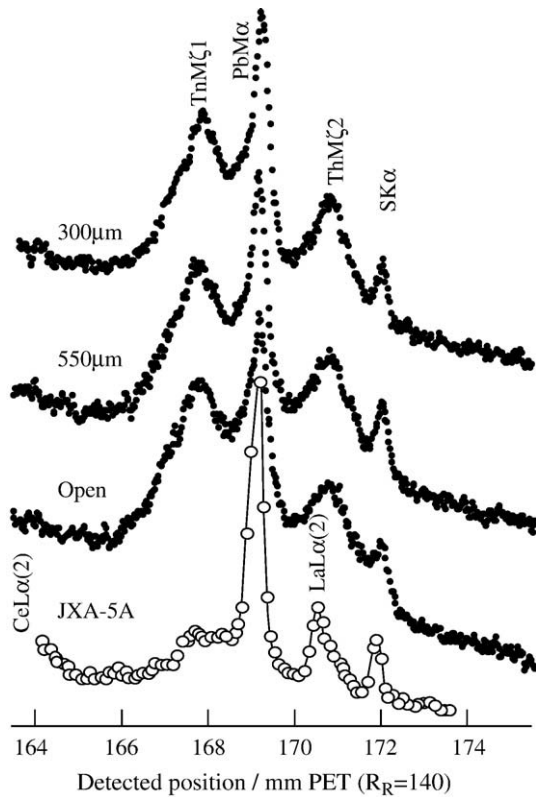
Fig. 1. Detailed WDS step scans around the PbMα region of monazite with collimators of 300 μm, 550 μm and 3 mm (open), together with the step scan obtained on the JEOL JXA-5A with a small sized PET crystal. The vertical intensity scale is arbitrary, and the horizontal axis represents the sample-diffraction crystal distance (mm) that is specified to the radius ($R_R = 140$ mm) of Rowland circle by L_{PET} (in mm) $= (R_R / d_{PET}) \times n\lambda$, where d_{PET} is the d-spacing of the PET (002) diffraction crystal (8.74 Å).

very low, Cocherie and Albarede (2000) ignored the parameter b and proposed new Th/Pb$=f$(U/Pb) representation, which is able to calculate the Th-age and U-age independently and then examine the concordance of the U–Pb age with the Th–Pb age. Th/Pb$=f$(U/Pb) is a simpler and graphically explicit 2-dimensional representation that makes this visualization easier.

3. EPMA hardware

3.1. Instrument

Variation in EPMA hardware has little effect on the resultant concentrations. However, certain difficulties that are normally unimportant in major element analyses become more acute in EPMA dating, i.e. accurate determination of Th, U and Pb concentration in minerals. The analytical protocols, therefore, must be developed with a specific EPMA in mind. All experimental results presented in this study were obtained by using JEOL JCXA-733 manufactured in 1984. The JCXA-733 employs a tungsten filament, and can achieve beam energies of 1–50 keV by 1 keV steps and beam current of 100 pA to 2 μA with probe diameters adjustable between 1 and 50 μm. It has 4 wavelength dispersive spectrometers (WDS) with a 140 mm radius of the Rowland circle, and individual WDS equips a PET

(002 pentaerythritol) diffraction crystal and a sealed Xe X-ray detector.

The spectral resolution of the JCXA-733 WDS compares unfavorably with that of JXA-5A WDS (Fig. 1), owing to the large-sized (30×12 mm) crystal of the Johann (1931) focusing arrangement. To minimize Bragg angle defocusing, X-ray collimator slits are placed between the diffraction crystal and the detector. Although there is no significant difference in U, Th, and Pb peak to background (P/B) ratio for different collimator width (Pyle et al., 2005a), improvement in the spectral resolution is carried out by adopting 0.55 mm or 0.3 mm collimator. The disadvantage of the collimator setting is a lowering in the count rate; the count rate and P/B ratio on the Pb-standard glass (PbO$=$10.18%, Suzuki and Adachi, 1998) at 15 keV are 5.13 cps/nA and 24 for collimator open (3 mm), 4.43 cps/nA and 29 for 0.55 mm collimator setting and 3.42 cps/nA and 33 for 0.3 mm collimator setting. Higher spectral resolution is desirable to enlarge spectral interference-free regions on continuum for background measurement as well as to minimize the
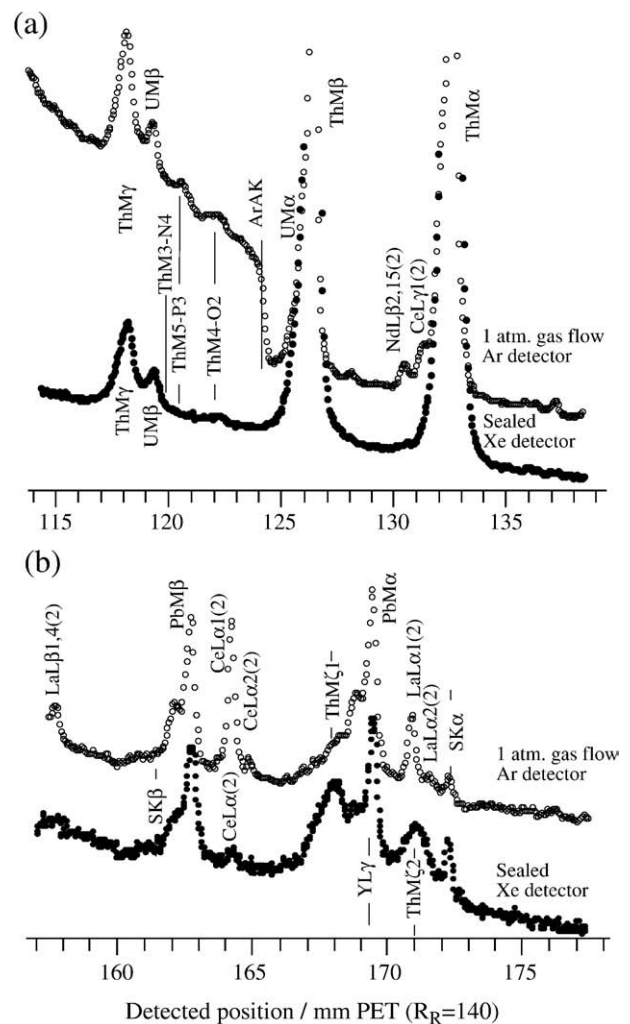

Fig. 2. Comparison of 1 atm gas flow Ar- and sealed Xe detector scans around ThMγ–ThMα (a) and PbMβ–PbMα (b) regions of monazite. The resolvable X-ray lines are indicated with notation. Explanation for vertical and horizontal axes is the same as in Fig. 1.
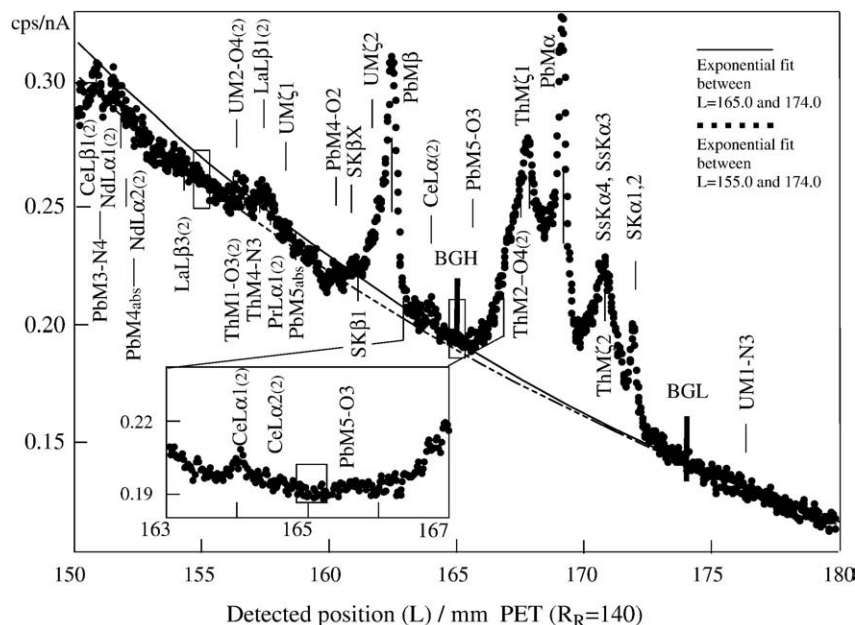
Fig. 3. Detailed WDS intensity step scan (40 s per point at 188 nA) for the Pb–M spectral region with PET crystal and sealed Xe detector on natural monazite. The insert enlarges the CeLα(2) to PbM5-O3 and shows presence of a narrow interference-free window at around 165 mm. Solid curve represents exponential regression on the basis of readings at c. 165 and 174 mm, and dashed curve does exponential regression on the basis of 155 and 174 mm readings. Explanation for horizontal axes is the same as in Fig. 1.

effects of spectral interferences such as ThMζ on PbMα and ThMγ on UMβ. We prefer 0.3 mm collimator setting to the wider setting for EPMA dating on the JEOL JCXA-733.

3.2. X-ray detector

Fig. 2 shows X-ray emission spectra around the ThMγ–ThMα and PbMβ–PbMα regions of monazite on both 1 atm gas flow Ar (P10) and sealed Xe (Xe–CO_2 with a low P_{Xe}) detectors. The Ar K-absorption edge appears at 3.871 Å (123.98 mm) between UMβ and UMα on the 1 atm Ar spectrum, resulting in a significant decrease in UMα, ThMβ and ThMα intensity relative to UMβ and ThMγ. Monazite contains La and Ce as major constituents. The wavelengths of second-order LaLα (5.33 Å) and CeLα (5.12 Å) are close to those of PbMα (5.29 Å) and PbMβ (5.07 Å), respectively. Particularly, the second-order
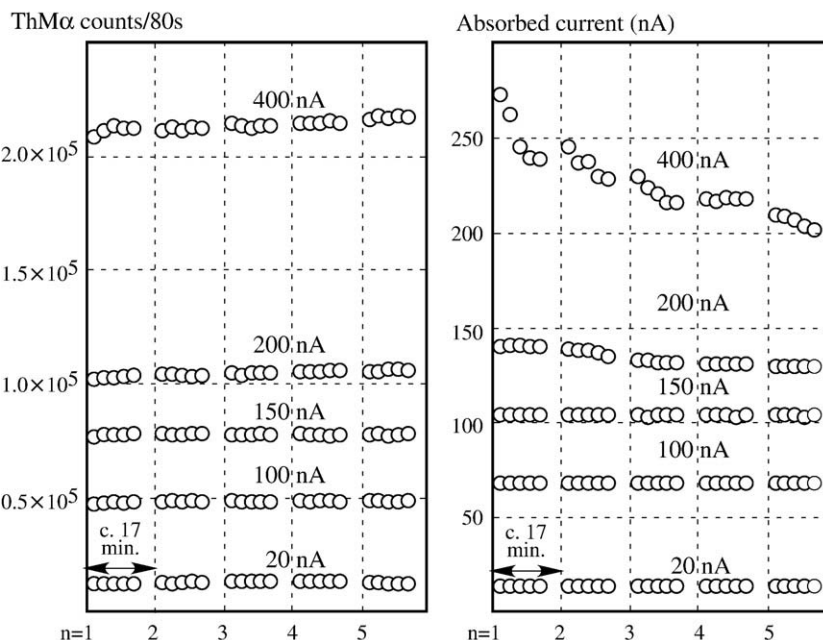

Fig. 4. ThMα X-ray intensity and absorbed current in monazite as a function of time and probe current at constant beam diameter of 3 μm. The carbon-coat thickness is about 25 nm, and the sampling period is 80 s. Five times high background (40 s) – peak (80 s) – low background (40 s) measurements of Th, U, Pb and Y followed by two high background (20 s) – peak (40 s) – low background (20 s) measurements of other elements need about 17 min (see the analytical sequence given in Fig. 9).

CeLα lines (CeLα1(2)=5.123 Å and CeLα2(2)=5.1412 Å) interfere with the spectral region between PbMβ (5.076 Å) and PbM5-O4 (5.168 Å), and prevent the selection of a small offset value for background determination. Because the energy of the Ar escape peak from CeLα (1.87 keV) overlaps partly the energies of PbMα (2.34 keV) and PbMβ (2.44 keV), the second-order CeLα lines are not filtered by pulse height analyzer. The Xe escape peaks from the second-order CeLα are largely excluded by the pulse-height window occupied by PbMα or PbMβ. This coupled with the adoption of 0.3 mm collimator slit provide us a narrow interference-free window between CeLα2(2) and PbM5-O3 (Fig. 3). Another interference-free window is located between LaLβ3(2) and ThM1-O3(2). The background value at the PbMα line position for a monazite with about 12 wt.% ThO$_2$ is 0.1677 cps/nA by exponential fit between 165 mm (0.1935± 0.0022 cps/nA) and 174 mm (0.1434±0.0019 cps/nA), and 0.1662 cps/nA by exponential fitting between 155 mm (0.2615± 0.0022 cps/nA) and 174 mm. The difference between those two exponential fittings is possibly due to the depression in count rate at the larger offset position through discrimination by the pulse-height window occupied by PbMα. Without a facility for automatic adjustment of the threshold and the window of the pulse-height analyzer, we select windows at 165 mm and 174 mm for the measurement of the monazite background at the PbMα line position. Linear interpolation between 165 and 174 mm gives a background of 0.1696 cps/nA at the PbMα position. Incidentally, the difference in background values between exponential and linear models corresponds 50–60 ppm in the PbO determination. Exponential fitting is desirable for background calculation of low Pb minerals as demonstrated by Jercinovic and Williams (2005). In the case of the same configuration of pulse-height analyzer for peak and offset positions, the exponential fitting potentially results in under estimation of background intensity, and linear interpolation gives a better approximation. A rigorous modeling of background determination is indispensable.

3.3. Accelerating voltage and electron beam current

Excitation efficiency depends on the overvoltage ratio (incident electron energy/critical excitation energy of a relevant shell). High accelerating voltage, therefore, is desirable to give the maximum count rate and the higher peak to background (P/B) ratio; the count rate and P/B ratio of PbMα on the Pb-standard glass (PbO=10.18 wt.%; Suzuki and Adachi, 1998) are 3.42 cps/ nA and 33 at 15 keV, 4.07 cps/nA and 36 at 20 keV and 5.42 cps/ nA and 38 at 25 keV, respectively. However, the X-ray generation volume in a sample rapidly increases with increasing incident electron energy. Pyle et al. (2005a) carried out Monte Carlo simulations of the electron interaction and X-ray generation volume in monazite at 15 keV and 25 keV, and showed that the radius of the volume is about 1 μm at 15 keV and 3 μm at 25 keV. Because Th- and U-bearing accessory minerals are compositionally inhomogeneous, we prefer 15 keV rather than higher accelerating voltages to obtain a high spatial resolution. An alternative way to the higher count rate is the adoption of a higher beam current. Almost the entire energy of the incident electron

beam is dissipated in the form of the heat at the point of irradiation, which may be sufficient to cause significant damage to the sample. Adopting a coating layer of higher thermal conductivity can reduce the temperature rise. Jercinovic and Williams (2005) showed that a 10 nm gold coating significantly reduces the surface damage with a small decrease in PbMα, UMβ and ThMα count rates relative to 25 nm carbon coating. Application of gold coating, however, generates a problematic AuMγ peak between the PbMβ and PbMα peaks. Further, the gold coating causes attenuation of incident electron energy (Osada, 2005; Kato, 2007) and a significant distortion in the depth distribution of X-ray generation (Kato, 2007), leading to inaccuracy in the quantitative matrix correction.

Fig. 4 shows the measured absorbed current and X-ray intensity of carbon-coated (c. 25 nm in thickness) monazite at 15 keV accelerating voltage and a defocused (3 μm) beam. With a 400 nA beam, the absorbed current decreases from 273 to 239 nA during five-160 s (80 s for peak plus two 40 s for background) sampling periods. In this experiment, the beam exposure was interrupted at every 17 min for a period of 2 s, and then resumed. The absorbed current decreased gradually during the first five-160 s of irradiation. It recovered incompletely during the 2 s interruption, and then decreased during the next five-160 s of irradiation. The behavior, as pointed out by Jercinovic and Williams (2005), suggests that the decrease in absorbed current is not a simple thermal effect. While the absorbed current decreases, the ThMα counts increases steadily; the count at the 25th 80 s peak counting interval is 1.03 times that of the first counting interval. These changes are accompanied by minor bright spotting on the monazite surface. Irradiation of 400 nA beam on metamict parts of monazite forms distinct crater with a significant variation in absorbed current and X-ray intensity. With a lower beam current, the absorbed current and X-ray count remains relatively constant for an exposure time over 85 min. A current as high as 400 nA coupled with defocused beam (3 μm in diameter) is acceptable for an exposure time exceeding 20 min. We normally adopt a 150–200 nA defocused (2–6 μm) beam, and integrate the X-ray intensity over a 300 to 600 s interval. As the response to beam irradiation is unique on individual parts of a single monazite grain, absorbed current and X-ray intensity must be monitored during the measurement if carbon is used as the conductive coating material.

3.4. Detection limits of electron microprobe analyses

The detection limits of the JCXA-733 were estimated from the correlation between the X-ray intensity and the element concentrations in a series of standard glasses whose compositions were determined by wet chemical and instrumental neutron activation analyses (Suzuki, 1987b). The calibration suggests that the practical limits of determination at 3σ confidence level are about 20 ppm for Cr. Further estimation shows that the intrinsic responses of the JCXA-733 counting systems with a PET crystal and a sealed Xe detector are around 0.8–0.9 cps/nA wt.% for ThMα, 0.7–0.6 cps/nA wt.% for UMβ and 0.37– 0.32 cps/nA wt.% for PbMα. The background counts on

monazite at the ThMα, UMβ and PbMα positions are 0.59–0.49, 1.02–0.92 and 0.18–0.13 cps/nA, respectively. By adopting a 400 s integration time and a 150 nA probe current, the detection limits of Pb, U and Th in monazite at 2σ confidence level are 100, 200 and 90 ppm, respectively.

3.5. X-ray lines used for Th, U and Pb determination and interferences

For analysis of Th, U and Pb in Th- and U-bearing minerals, M lines are preferable to L lines, because the critical excitation energy for the L-shells of Th and U are higher than 15 keV. Fig. 5 shows the X-ray emission spectra in the ThMγ–ThMα region for monazite, xenotime, zircon and polycrase.

The ThMα (4.14 Å) line can be measured without significant interferences for most Th- and U-bearing accessory minerals. Incidentally, this line experiences interference from AgLα (4.15 Å) line. Carbon paint, therefore, is preferable to silver paint for affixing a polished thin section on the sample holder. The UMα (3.91 Å) lined is overlapped by the ThMβ (3.94 Å) line
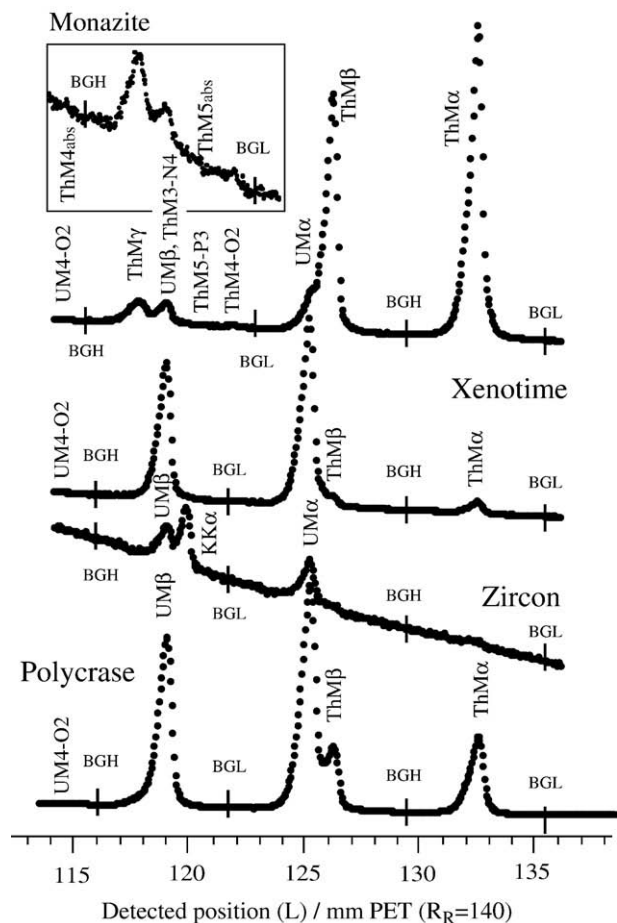

Fig. 5. Detailed WDS intensity step scans around the ThMγ–ThMα region of monazite, xenotime, zircon and polycrase with a PET crystal and sealed Xe detectors. The main X-ray lines are indicated with notation. Vertical broad lines show positions chosen for background measurement. Note that the background under the line peak is approximated by linear interpolation of BGH and BGL. Explanation for vertical and horizontal axes is the same as in Fig. 1.
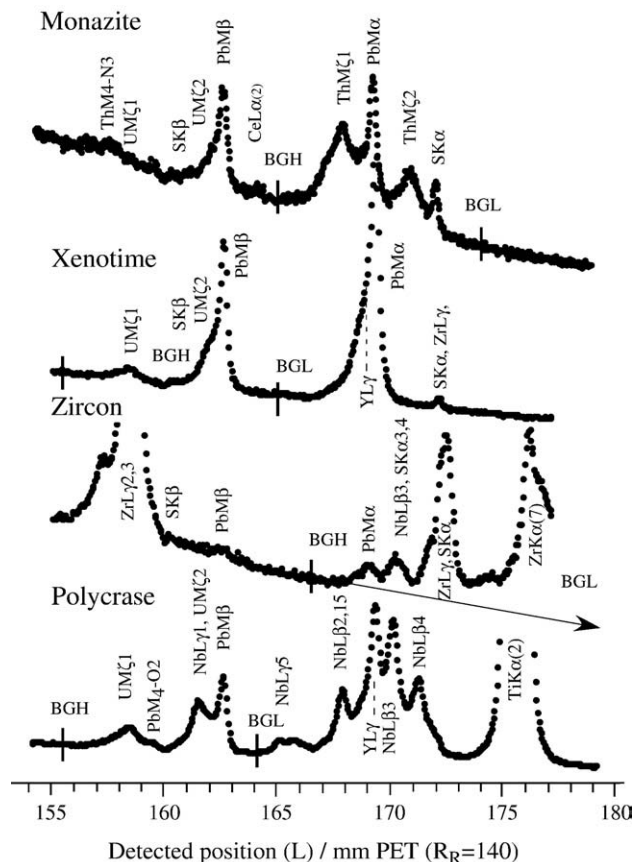

Fig. 6. Detailed WDS intensity step scans around the PbMβ–PbMα region of monazite, xenotime, zircon and polycrase with a PET crystal and sealed Xe detectors. The resolvable X-ray lines are indicated with notation. Explanation for vertical and horizontal axes is the same as in Fig. 1.

and is rarely used for determination of U in Th-rich minerals. The UMβ (3.716 Å) line is overlapped by the ThMγ (3.679 Å), ThM3-N4 (3.718 Å), ThM5-P3 (3.760 Å), KSKα4 (3.716 Å), KSKα3 (3.721 Å) and KKα1,2 (3.742 Å) lines and the ThM5 absorption edge (3.729 Å). In general, Th- and/or U-bearing accessory minerals do not contain detectable amount of K. Therefore, analytical results are discarded, when a significant amount of K (e.g. usually over 0.06 wt.% K_2O) is measured. Interference of 0.06 wt.% K_2O on UMβ is negligibly small, around 0.002 wt.% UO_2. The combined effect of ThMγ, ThM3-N4 and ThM5-P3 lines on UMβ can be corrected through the procedure described in Åmli and Griffin (1975):

$$I_{UM\beta}(net) = I_{UM\beta}(obs) - I_{ThM\alpha}(obs) \times f_{ThM\gamma} \quad \text{(in sample)} \tag{11a}$$

where $f_{ThM\gamma}$ is the correction factor and is defined as:

$$f_{ThM\gamma} = I(obs) \text{ at } UM\beta \text{ detected position}$$

$$/I_{ThM\alpha}(net) \text{ (in pure } ThO_2 \text{ or U-free Th standard).} \tag{11b}$$

Unfortunately, pure ThO_2 or synthesized U-free Th standards are difficult to obtain in Japan due to legal regulations. We estimate the correction factor with Th-rich and U-poor monazite.

If monazite contains over 25 wt.% ThO_2 and a barely detectable amount of UO_2 (no intensity increase at $UM\beta$ line position; readers are requested to refer Fig. 5 of Suzuki, 2005), the $f_{ThM\gamma}$ value measured on monazite will be approximate to that measured on pure ThO_2 or synthesized U-free Th standards, with typical value of $f_{ThM\gamma}$ around 0.0073. Alternatively, the "working standard" technique developed by Kato et al. (2005) is adopted to eliminate the interference correction. The solid lines labeled with BGH and BGL are the segments for background measurement. Continuous X-ray emission has a curved intensity distribution (Jercinovic and Williams, 2005; Pyle et al., 2005a). However, our experiments show that there is no significant difference in background estimates by linear interpolation and exponential fitting for the case of small offset positions, BGH and BGL.

Fig. 6 shows wavelength step scan of the $PbM\beta$ to $PbM\alpha$ regions of monazite, xenotime, zircon and polycrase. Both PbM lines are subject to several first order interferences. The $PbM\alpha$ line is overlapped severely by $YL\gamma2,3$ line. Other interferences for $PbM\alpha$ arise from $ThM\zeta1$, $ThM\zeta2$, $SK\alpha3,4$ and $NbL\beta3$ lines. The $PbM\beta$ line is overlapped by $UM\zeta2$ and $NbL\gamma$ lines. Lead is present in much lower abundance than Th and U in Th- and U-bearing minerals, especially young ones, and Pb analytical precision controls the precision of the estimated age. The $PbM\alpha$ line as measured on the JCXA-733 is approximately 25% more intense than the $PbM\beta$ line. The $PbM\beta$ line has a disadvantage in evaluation of background, because its high-energy side is occupied by a series of $NbL\gamma$, $UM\zeta2$, $PbM_4\text{-}O2$ and $SK\beta$ lines and by second-order $L\alpha$ and $L\beta$ lines of rare earth elements. We, therefore, use the $PbM\alpha$ line for the Pb determination of monazite and zircon. The interferences are empirically corrected by

$$I_{PbM\alpha}(net) = I_{PbM\alpha}(obs) - I_{NbL\alpha}(obs) \times f_{NbL\beta} - I_{YL\alpha}(obs)$$
$$\times f_{YL\gamma} - I_{ThM\alpha}(obs) \times f_{ThM\zeta} - I_{SK\alpha}(obs) \times f_{SK\alpha}$$
$$(12a)$$

where $f_{NbL\beta}$, $f_{YL\gamma}$ and $f_{ThM\zeta}$ are the correction factors and are defined as

$$f_{NbL\beta} = I(obs) \text{ at } PbM\alpha \text{ detected position}$$
$$(12b)$$
$$/I_{NbL\alpha}(obs) \text{ (in columbite standard)}$$
$$f_{YL\gamma} = I(obs) \text{ at } PbM\alpha \text{ detected position} \qquad (12c)$$
$$/I_{YL\alpha}(obs) \text{ (in Y-bearing glass standard)}$$

$$f_{ThM\zeta} = \{I_{PbM\alpha}(obs,mz\text{-}std) - I_{PbM\beta}(obs,mz\text{-}std) \qquad (12d)$$
$$\times I_{PbM\alpha}(obs,Pb\text{-}std)/I_{PbM\beta}(obs,Pb\text{-}std)\}$$
$$/I_{ThM\alpha}(obs,mz\text{-}std)$$
$$\text{(in a high Th and low U monazite standard}$$
$$\text{and in a U- and Th-free Pb standard)}$$

$$f_{SK\gamma} = I(obs) \text{ at } PbM\alpha \text{ detected position} \qquad (12e)$$
$$/I_{SK\alpha}(obs) \text{ (in barite standard).}$$

The values of $f_{NbL\beta}$, $f_{YL\gamma}$, $f_{ThM\zeta}$ and $f_{SK\gamma}$ are machine-dependent, and are typically around 0.0135, 0.0089, 0.00099 and 0.00061, respectively. Normally, monazite and zircon contain little Nb, and the correction of the $NbL\beta$ interference is insignificant. Because $YL\gamma$ interference with $PbM\alpha$ is severe for xenotime and polycrase, the $PbM\beta$ line is used for Pb determination in these minerals. This line is interfered by $NbL\gamma$, $UM\zeta2$ and a series of $SK\beta$ lines. Normally xenotime and polycrase analyses showing detectable amounts of S are not used for age calculation. Therefore, the $NbL\gamma$ and $UM\zeta2$ interferences only are corrected by,

$$I_{PbM\beta}(net) = I_{PbM\beta}(obs) - I_{UM\alpha}(obs) \times f_{UM\zeta}$$
$$- I_{NbL\alpha}(obs) \times f_{NbL\gamma} \qquad (13a)$$

where $f_{NbL\gamma}$ and $f_{UM\zeta}$ are the correction factors and are defined as:

$$f_{UM\zeta} = \{I_{PbM\beta}(obs,xe\text{-}std) - I_{PbM\alpha}(obs,xe\text{-}std) \qquad (13b)$$
$$\times I_{PbM\beta}(obs,Pb\text{-}std)/I_{PbM\alpha}(obs,Pb\text{-}std)\}$$
$$/I_{UM\beta}(obs,xe\text{-}std)$$
$$\text{(interference corrected value in a high U}$$
$$\text{and low Th xenotime standard and in a}$$
$$\text{U- and Th-free Pb standard)}$$

$$f_{NbL\gamma} = I(obs) \text{ at } PbM\beta \text{ detected position} \qquad (13c)$$
$$/I_{NbL\alpha}(obs) \text{ (in columbite standard)}$$

The $f_{UM\zeta}$ and $f_{NbL\gamma}$ values are typically around 0.00186 and 0.007, respectively. Monazites from some sample contain

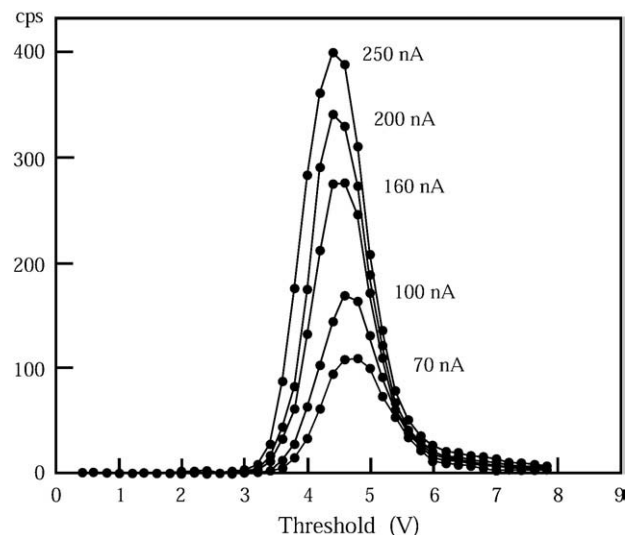Fig. 7. Single-channel analyzer step scans of monazite (c. 15 wt.% ThO_2) with spectrometer at $ThM\alpha$ position and a window width of 0.5 V under different probe currents from 70 to 250 nA.

significant amount of sulfur, the S content range as high as 1 wt.%. Correction of SKβ1 and SKβX interferences is indispensable if the PbMβ is the line selected for Pb determination of monazite. The correction factor for the combined SKβ1 and SKβX interferences is typically around 0.00175.

3.6. Standards

Standards used in CHIME dating are euxenite provided by Smellie et al. (1978) for Th, U and Nb, synthesized glass provided by Suzuki and Adachi (1998) for Pb, Si and Ca, synthesized Y-glass (Y_2O_3 = 10 wt.% and K_2O = 2 wt.%) for Y and K, barite for S, zirconia for Zr, and xenotime for P. A high Th monazite with little U is used to determine the X-ray correction factors $f_{ThM\gamma}$ (Eq. (11b)) and $f_{ThM\zeta}$ (Eq. (12d)), and a high U xenotime with little Th is used to determine $f_{UM\zeta}$ (Eq. (13b)). The correction factor for Nd interference is estimated by using inhomogeneous columbite (Nb_2O_5 = 31–36 wt.%). Standards for rare earth elements, when analyzed, are synthetic glass provided by Drake and Weill (1972).

All standards we used are in low concentrations. With standards of high concentrations, measurements of standards and unknown samples are normally performed at different probe currents. This procedure is sometimes unreliable, because of the non-linearity of the ammeter. Ammeters of electron microprobe analyzers cover a wide range (10^{-12} to 10^{-5} A) of probe current by changing the range registers. Because the precision of registers is in the order of ±1%, the linearity of ammeters over different ranges is not guaranteed on the JCXA-733. We normally measure both standards and unknown samples at the same probe current. The low-concentration standards can be measured at reasonable count rates under a high probe current, 100–200 nA, needed for analyses of trace-level Pb.

In the case of high-concentration standards, a pulse from single channel analyzer can shift to lower voltage with increasing count rate (Pyle et al., 2005a). Energy step scans of pulse-height analyzer under various probe current conditions reveal a significant pulse shift (Fig. 7). The X-ray entering the detector ionizes counter gas to generate free electron–ion pairs. Since the mobility of positive ions is 1000 times slower than the faster moving electrons, the ions form a space-charge shield around the anode wire (Geller and Herrington, 2002). This reduces temporally the counter voltage and we can see the effect as pulse shrinkage when going to a higher count rate. Normally adjustment of the pulse-height analyzer is carried out on a standard under higher count-rate conditions to ensure the 95% confident level setting of the threshold and the window. Enlargement of the window size coupled with lowering the threshold, in practice, can minimize the pulse shrinkage problem. This configuration is also effective in minimizing the depression in count rate on the large offset positions during background determination (see Section 3.2).

4. Measurements

4.1. Sample preparation

EPMA analyses are carried out on in-situ mineral grains in a polished thin section, or physically separated mineral fractions embedded in epoxy grain-mounts.

Polished thin sections were prepared by conventional procedures making samples suitable for EPMA analysis. As the presence of surface relief causes loss of continuity of the coating film and results in a charging effect and rising temperature, surface relief should be reduced carefully by polishing with 5 μm Al_2O_3 powder on an agate plate and then with 0.5 and 0.25 μm diamond powder on Doctor-Lap rotary polishers. A distinct advantage of this approach is that the textural relations can be observed: it is helpful in interpreting the derived ages.

Th- and U-bearing minerals are very sparse in some samples such as sandstone. For such samples, mounts of separated grains are favorable over polished thin sections for EPMA dating. Samples of around 1 kg, sometimes more than 10 kg, were crushed on a stamp mill. The size reduction was undertaken only
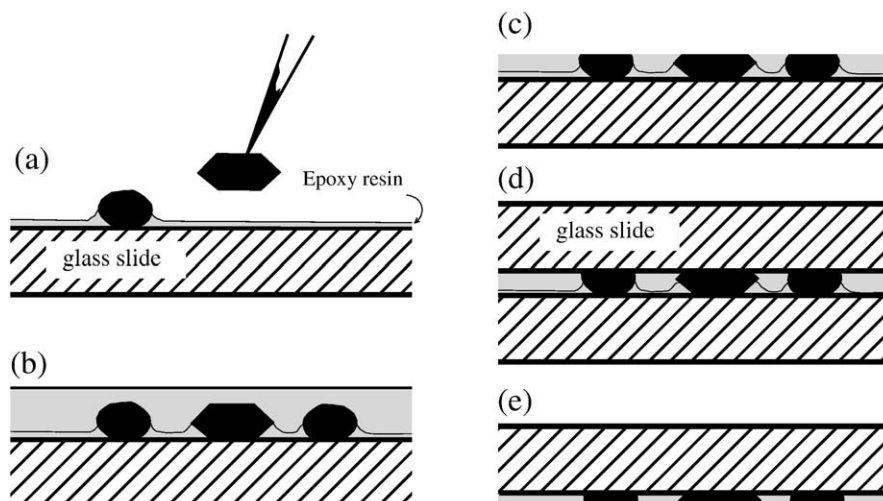

Fig. 8. Mounting of separated grains on a glass slide (a), covering with epoxy resin (b), grinding with 15 and 5 μm Al_2O_3 powder to one third in thickness (c), remounting on a glass slide (d), and grinding the first glass slide followed by polishing with 15 and 5 μm Al_2O_3 and further with 0.5 and 0.25 μm diamond powder (e).

Fig. 9. Analytical sequence of the CHIME dating (left) and an example of the analytical output (right). Monazite and allanite analyses skip the ZrLα measurement, and xenotime and polycrase analyses prefer PbMβ to PbMα. Elemental combination is optimized to make minimum displacement of analyzing crystals on the JCXA-733 spectrometer. Absorbed current is monitored after every U, Th, Pb and Y peak measurements and printed out. Italics give explanations for the output sheet.

to the extent necessary for disaggregation of monazite through periodic sieving to remove undersized (−60 mesh) particles before further reduction of oversized ones. The heavy fraction including Th- and U-bearing minerals was concentrated from each sieved sample by panning to a purity of about 80%. Normally, further concentration by using heavy liquid was not
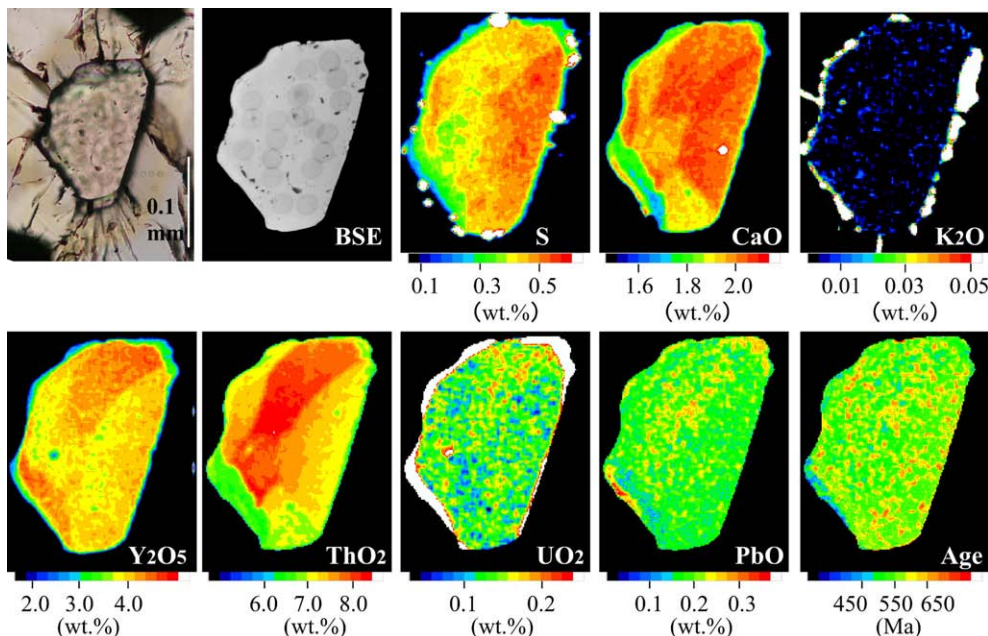

Fig. 10. Sulfur compositional map together with photomicrograph (plane polarized light), BSE image, a chronological map for S-bearing monazite in migmatite from India. Analytical conditions for this mapping were 15 keV, 300 nA and 2 s dwell time for the S, Ca, K and background measurement, 300 nA and 4 s dwell time for the Th, U, Pb and Y measurement, and pixel step=2 μm.

done. The concentrates were washed with dilute HCl and purified on an isodynamic magnetic separator. Mineral grains were hand-picked under a binocular microscope, divided for every size, mounted on a glass slide with an epoxy resin (Fig. 8a), and dried on a hot plate at 150 °C. After covering with more epoxy resin (Fig. 8b) and drying, the samples were polished with 15 and 5 μm Al₂O₃ powder until the grains were thinned approximately to one third in thickness (Fig. 8c). This flat surface was mounted on a glass slide with epoxy resin; the sample is sandwiched between two slides (Fig. 8d). The first glass slide was removed by grinding, and the exposed side was then polished with 15 and 5 μm Al₂O₃ on an agate plate and further with 0.5 and 0.25 μm diamond powder on a Doctor-Lap rotary polisher to expose midsections (Fig. 8e). This approach is desirable to make mineral sections with rather constant thickness, which can be helpful in observation of internal structure of individual grains under a polarizing microscope.

The polished sections were then photographed in plane and transmitted light, and also examined on a polarizing microscope in order to identify compositional and textural variations, in-clusions, internal cracks and metamict alternation within grains. Plane and transmitted light images of individual grains were obtained to aid in spot location. The samples were cleaned in a surfactant solution, thoroughly rinsed in de-ionized water and dried. The samples were then covered with roughly 25 nm of carbon with JEOL JEE-420 vacuum evaporator.

4.2. Spot by spot analyses

If monazite contains 10 wt.% ThO_2, the PbO accumulated during a 100 Ma time span is 421 ppm (c. 390 ppm Pb). With a PET crystal and a sealed Xe detector, the responses of the JCXA-733 counter system at 15 keV are around 0.34 cps/nA wt.% Pb for $PbM\alpha$ and 0.15 cps/nA for background of monazite. To analyze 420 ppm PbO at 1σ counting error of 10% with 160 nA probe current, a counting duration over 400 s is needed for peak and background. As noted above, long irradiation of a high-current beam sometimes changes the sample surface, recognized by a decreasing specimen current coupled with spotting and cratering. To monitor the specimen current, we normally repeat the measurement of peak and background positions five times for the simultaneous analysis of Th, U, Pb and Y (Fig. 9). In addition to these age equation components, our analytical schedule includes elements required for interference correction or for evaluation of analyzing data set. $CaK\alpha$, $SK\alpha$, $PK\alpha$, $KK\alpha$, $SiK\alpha$ and $NbL\alpha$ lines are also measured for monazite, xenotime, euxenite–polycrase and allanite analyses. $ZrL\alpha$ is added for zircon and xenotime analyses.

Every data set showing a significant variation of absorption current or extraordinarily high $KK\alpha$ counts (corresponding to over 0.06 wt.% K_2O) is discarded. After correction of back-ground and interferences, the X-ray intensity data are calibrated with the intensity data of standards. The relative intensities are converted into concentrations through the Bence and Albee (1968) method using an α-factor table calculated by Kato (2005) from the full PAP correction and compositions of natural monazite, xenotime, zircon, polycrase and allanite as refer-
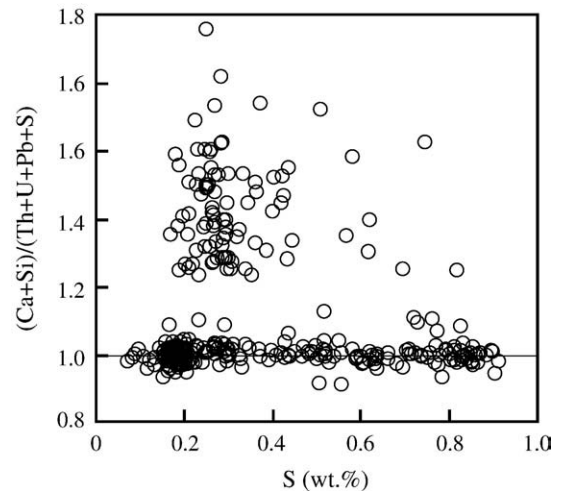

Fig. 11. Plots of the (Ca+Si)/(Th+U+Pb+S) atomic ratio against the S concentration for S-bearing monazite as old as c. 1500 Ma from a variety of rocks.

ences. The small difference in the matrix between the reference and analyzed minerals has little effect on the ThO_2, UO_2 and PbO determinations, and the maximum error in this calculation, normally around 0.5% of the concentration, is less than the uncertainty in the X-ray counting (Suzuki, 2005).

4.3. Chemical criteria of possibly discordant age data

Monazite grains in some samples contain intrinsically sig-nificant amounts of sulfur (Cressey et al., 1999; Jercinovic and Williams, 2005), while monazite grains in most samples do not contain a detectable amount of S. The S content varies as high as 0.9 wt.% in S-bearing monazite. Fig. 10 shows distribution of S within a monazite grain in a pelitic migmatite from southern India, together with photomicrographs and intragrain distribution of CaO, K_2O, Y_2O_3, ThO_2, UO_2 and PbO and age. In the S-distribution map, white spots along the monazite margin represent iron sulfide. The S content of the monazite grain ranges between 0.18 and 0.56 wt.%, and appears to be covariant with Ca. Ca in monazite is most commonly present as a brabantite (($Th,U)Ca(PO_4)_2$) component. Moreover, Th also forms the huttonite (($Th,U)SiO_4$) substitution. Therefore the amount of Ca that is available for other type of coupled substitution can be approximated by Ca+Si−(Th+U+Pb). As shown in Fig. 11, the (Ca+Si)/(Th+U+Pb+S) atomic ratios are in unity, confirming that coupling of S and Ca is a dominant substitution set in S-bearing monazites. Within a single mona-zite domain, data sets with (Ca+Si)/(Th+U+Pb+S) ratios close to unity give apparent ages (calculated by Eq. (5)) of a limited range, while those showing large deviation of the (Ca+Si)/(Th+U+Pb+S) ratios from unity give highly variable ap-parent ages. The large deviation in the (Ca+Si)/(Th+U+Pb+S) ratios are encountered for spots on "hidden fractures" and "hidden holes" that appear after long irradiation of high beam dose but are not detected by optical microscope and BSE before spot analyses, as well as for spots on metamict portions. Although the atomic proportion in monazite is further

Table 1
Microprobe analyses of monazites in a paragneiss sample (KS-01081705B) from the sillimanite–orthoclase zone of the Gyeonggi Massif in the Chungchon area, Korean Peninsula

Spot no.	ThO_2	UO_2	PbO	Age	ThO_2*	CaO	Y_2O_3	S	K_2O	SiO_2	CS/TUPS
M01-01	4.70	0.241	0.0606	261	5.48	0.85	1.53	nd	0.047	0.24	1.02
M01-02	3.19	0.706	0.0550	237	5.48	0.72	1.06	nd	1.719	17.45	20.28
M01-03	2.76	0.769	0.0553	249	5.25	0.53	0.66	nd	2.030	20.22	25.57
M01-04	6.38	0.261	0.0775	253	7.22	0.94	1.51	nd	0.045	0.48	0.97
M02-01	5.22	0.254	0.0645	252	6.04	0.77	1.02	nd	0.084	0.44	1.00
M02-02	5.27	0.244	0.0614	239	6.06	0.72	0.93	nd	0.057	0.94	1.35
M03-01	3.26	0.954	0.0673	250	6.36	0.49	0.60	0.01	3.384	11.49	12.34
M03-01	2.06	1.300	0.0468	177	6.25	0.36	0.41	nd	4.530	17.11	22.69
M04-01	5.65	0.375	0.0792	273	6.86	0.95	1.47	nd	0.021	0.34	0.98
M04-02	5.47	0.323	0.0720	261	6.52	0.99	1.52	nd	0.043	0.29	1.01
M04-03	5.50	0.352	0.0716	255	6.65	0.99	1.52	nd	0.031	0.27	0.98
M04-04	5.64	0.384	0.0741	254	6.89	0.95	1.54	nd	0.022	0.34	0.98
M04-05	5.09	0.301	0.0665	259	6.06	0.88	1.29	nd	0.035	0.29	1.00
M05-01	15.58	0.473	0.1905	263	17.11	1.90	0.58	nd	0.040	1.56	0.97
M05-02	18.21	0.500	0.2052	245	19.83	2.30	0.60	nd	0.032	1.72	0.97
M05-03	20.71	0.584	0.1900	199	22.60	2.19	0.61	nd	0.028	2.07	0.90
M05-04	19.23	0.519	0.2203	249	20.91	2.09	0.63	0.01	0.034	2.29	1.00
M05-06	16.54	0.491	0.1946	254	18.13	2.01	0.66	nd	0.038	1.78	1.00
M05-07	14.56	0.441	0.1212	179	15.99	2.05	0.63	nd	0.053	2.31	1.31
M05-08	10.24	0.328	0.0976	204	11.30	1.75	0.75	nd	0.061	0.52	0.98
M05-09	2.81	0.860	0.0458	194	5.59	0.59	0.33	nd	1.536	25.61	31.10
M05-10	2.46	0.632	0.0414	218	4.50	0.50	0.33	nd	1.032	26.44	37.95
M05-11	19.02	0.550	0.1503	171	20.80	2.13	0.61	nd	0.033	1.56	0.85
M05-12	21.47	0.589	0.2464	249	23.38	2.43	0.59	nd	0.025	2.31	0.97
M05-13	20.63	0.547	0.1623	171	22.39	2.16	0.62	nd	0.035	1.92	0.87
M05-14	10.51	0.341	0.1209	246	11.61	1.67	0.86	nd	0.033	0.74	1.01
M05-15	10.95	0.332	0.1324	260	12.03	1.74	0.70	nd	0.043	0.66	0.97
M05-16	11.64	0.564	0.0844	148	13.46	1.63	0.69	nd	0.423	6.67	3.01
M06-01	3.96	0.763	0.0718	263	6.44	0.78	0.47	nd	1.997	23.86	22.62
M06-02	3.19	0.306	0.0299	170	4.17	0.64	0.34	nd	0.912	35.63	45.32
M07-01	3.54	0.366	0.0488	244	4.73	0.64	0.57	nd	0.040	0.19	0.98
M07-02	3.59	0.347	0.0525	263	4.71	0.65	0.55	nd	0.039	0.19	0.97
M07-03	3.94	0.358	0.0546	253	5.10	0.70	0.53	nd	0.043	0.22	0.97
M08-01	5.54	2.405	0.1433	254	13.34	1.55	2.13	nd	0.019	0.15	0.99
M08-02	5.49	1.979	0.1134	225	11.90	1.43	2.13	0.03	0.136	0.66	1.28
M08-03	5.66	2.723	0.1557	254	14.49	1.68	2.24	nd	0.034	0.13	1.00
M08-04	5.41	1.566	0.1099	248	10.48	1.32	2.21	nd	0.015	0.19	1.00
M08-05	6.37	1.380	0.1225	267	10.84	1.49	2.07	nd	0.030	0.30	1.06
M08-06	5.93	1.182	0.1006	244	9.76	1.22	2.12	nd	0.021	0.36	1.02
M08-07	5.90	1.955	0.1406	271	12.25	1.38	2.27	nd	0.034	0.25	0.95
M08-08	7.04	0.837	0.1025	248	9.75	1.10	2.04	nd	0.016	0.64	1.00
M08-09	5.25	1.631	0.1110	249	10.54	3.18	1.98	nd	0.044	0.93	2.73
M09-01	6.84	0.685	0.0963	251	9.06	0.94	2.13	nd	0.014	0.76	1.02
M09-02	6.06	0.534	0.0851	258	7.79	0.73	1.98	nd	0.018	0.69	0.97
M09-03	5.46	0.509	0.0771	256	7.11	0.80	2.04	nd	0.023	0.54	1.01
M09-04	5.26	0.501	0.0724	249	6.88	0.73	1.99	nd	0.034	0.52	0.98
M09-05	5.77	0.696	0.0875	258	8.03	0.97	2.08	nd	0.042	0.48	1.01
M09-06	6.74	0.587	0.0947	259	8.64	0.85	2.01	nd	0.014	0.82	1.03
M09-07	5.49	0.698	0.0817	249	7.75	0.92	2.08	nd	0.035	0.46	1.01
M09-08	5.96	0.579	0.0850	256	7.84	0.89	2.04	nd	0.021	0.51	0.97
M10-01	6.08	1.771	0.1289	258	11.82	1.53	2.13	nd	0.042	0.23	1.03
M10-02	8.73	0.736	0.1149	244	11.11	1.17	2.16	nd	0.028	0.90	0.99
M10-03	5.98	0.742	0.0832	234	8.39	1.01	2.19	nd	0.023	0.53	1.04
M10-04	5.99	0.789	0.0992	274	8.55	1.06	2.10	nd	0.013	0.46	1.02
M10-05	5.34	0.563	0.0755	249	7.16	0.83	2.17	nd	0.008	0.50	1.02
M10-06	6.03	1.872	0.1338	261	12.11	1.30	2.19	nd	0.014	0.41	0.98
M10-07	6.00	0.730	0.0895	253	8.37	1.08	2.08	nd	0.014	0.43	1.02
M10-08	5.87	0.568	0.0852	261	7.71	0.89	2.17	nd	nd	0.56	1.02
M10-09	5.52	0.575	0.0759	243	7.38	0.89	2.08	nd	0.006	0.49	1.02
M10-10	6.25	1.373	0.1180	260	10.71	1.34	2.17	nd	0.009	0.31	0.99
M10-11	5.58	0.597	0.0787	248	7.51	0.88	2.11	nd	0.007	0.52	1.02
M11-01	6.13	0.641	0.0832	240	8.21	0.93	2.20	nd	0.033	0.58	1.01
M11-02	6.49	0.624	0.0950	263	8.52	0.96	2.25	nd	0.026	0.61	1.00

Table 1 (continued)

Spot no.	ThO$_2$	UO$_2$	PbO	Age	ThO$_2$*	CaO	Y$_2$O$_3$	S	K$_2$O	SiO$_2$	CS/TUPS
M11-03	3.72	1.636	0.0706	185	9.00	0.98	0.98	nd	0.297	24.90	21.09
M12-01	8.47	0.797	0.1172	250	11.06	1.45	2.10	nd	0.008	0.62	1.01
M12-02	8.34	0.790	0.1238	268	10.91	1.43	2.08	nd	0.010	0.62	1.02
M12-03	7.30	0.630	0.0991	251	9.34	1.12	2.05	nd	0.032	0.62	1.00
M12-04	7.98	0.651	0.1117	262	10.09	1.08	2.38	nd	0.008	0.85	1.01
M12-05	5.22	0.350	0.0614	228	6.36	0.61	0.98	0.01	0.011	8.97	7.50
M12-06	7.77	0.639	0.1087	261	9.84	1.12	2.25	nd	nd	0.75	1.01
M12-07	6.82	0.567	0.0954	260	8.66	0.94	2.19	nd	0.011	0.71	1.01
M12-08	7.23	0.617	0.0996	255	9.23	1.08	2.18	nd	nd	0.69	1.02
M12-09	6.49	0.577	0.0923	261	8.36	0.94	2.11	nd	0.020	0.64	1.01
M13-01	11.84	0.644	0.1469	249	13.93	1.28	2.18	nd	0.013	1.46	0.98
M13-02	10.08	0.776	0.1348	253	12.59	1.47	2.25	nd	0.015	0.89	0.98
M13-03	9.94	0.759	0.1276	243	12.40	1.48	2.29	nd	0.025	0.93	1.02
M13-04	12.73	0.688	0.1626	257	14.96	1.32	2.21	nd	0.013	1.70	1.00
M13-05	9.26	0.639	0.1283	267	11.34	1.18	2.36	nd	0.006	1.03	1.00
M13-06	13.93	0.754	0.1810	261	16.38	1.48	2.23	nd	0.014	1.75	0.98
M14-01	8.93	2.933	0.1997	256	18.44	2.14	2.31	nd	0.051	0.44	1.00
M14-02	13.31	0.838	0.1750	258	16.03	1.94	2.27	nd	0.024	1.25	1.02
M14-03	16.16	1.016	0.2135	259	19.46	1.66	2.53	nd	0.024	2.16	0.99
M14-04	10.48	1.444	0.1662	259	15.16	1.92	2.25	nd	0.037	0.65	0.98
M14-05	9.92	2.630	0.1942	249	18.45	2.45	2.37	nd	0.030	0.27	1.00
M14-06	10.67	0.622	0.1287	240	12.69	11.38	1.80	nd	0.010	1.13	5.12

CS/TUPS: the molar (CaO+SiO$_2$)/(ThO$_2$+UO$_2$+PbO+S) ratio and nd: below the detection limit.

affected by minor substitution by halogens (Andreoli et al., 1994) and Sr (Chakhouradian and Mitchell, 1998), the (Ca+Si)/(Th+U+Pb+S) ratio becomes a temporal criterion for discordance in S-bearing monazite.

Within S-free monazite, limited spots only show small amounts of S that is fixed at least partly in iron sulfide or galena of submicron size. Further, the (Ca+Si)/(Th+U+Pb+S) atomic ratios deviate from unity for spots in metamict portions. The chemical features provide a practical discrimination of analyses on possibly discordant domains from those on concordant domains.

Table 1 lists analytical data from monazite grains in a paragneiss of sillimanite–orthoclase grade in the Gyeonggi massif of the Korean Peninsula. Monazite grains are small in size (mostly smaller than 50 μm), and contain tiny mica, quartz and feldspar inclusions, microfractures and metamict domains. Although all data suit the criterion of constant absorbed current, they yield a complex cloud on the PbO vs. ThO$_2$* diagram (Fig. 12a), and it is hard to obtain reasonable isochron age. As shown in Table 1, some data sets show extraordinary high SiO$_2$ contents coupled with high K$_2$O contents, and may arise from analyzing on and/or around inclusions. Chemical data provide additional information to construct an isochron free of potentially discordant data points. Fig. 12b emphasizes data points with the (Ca+P)/(Th+U+Pb+S) ratio of 0.95–1.05 and no sulfur. The filtered data points, except M05-08, are arrayed
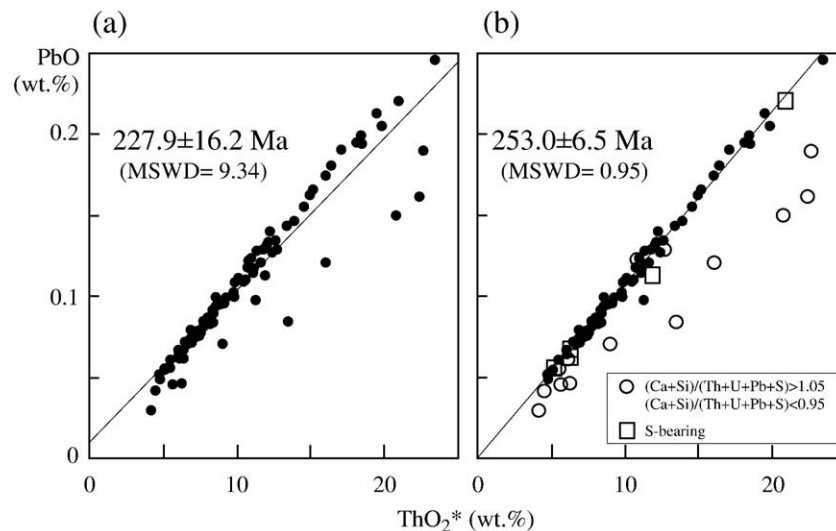

Fig. 12. PbO vs. ThO$_2$* (ThO$_2$ plus the equivalent of UO$_2$) plot of 85 analyses on 14 monazite grains (Table 1). Data points disperse significantly, and the regressed isochron has significant scatter (left). Data points with the (Ca+Si)/(Th+U+Pb+S) ratio of 0.95–1.05 are highlighted in the right. The filtered data set array linearly and yield a well-defined isochron.

linearly. The M05-08 spot shows a high K_2O concentration (0.061 wt.%), and the apparent age of 204 Ma lies outside of the 95% confidence interval around the average. Similarly, the M02-01 spot shows 0.084 wt.% K_2O. It is highly possible that the domains for M05-08 and M02-01 underwent chemical alteration and are outlier. Data points on possibly concordant domains yield a well-defined isochron of 253.0 ± 6.5 Ma.

Geisler and Schleicher (2000) found that the apparent age (*t*) of zircon decreases systematically with increasing Ca contents, and ages on domains containing less than 0.2 wt.% CaO agree with conventional radiometric ages of the host rocks. Fig. 13 shows distribution of Ca within a single zircon grain in hornblende-bearing biotite granite from Madagascar. Most parts of the grain are transparent under the microscope, but the lower right margin is translucent owing to metamictization. The BSE image shows two dark zones with a euhedral habit. Calcium concentrates extensively in the dark zone, and less extensively along fractures and in the metamict lower right margin. The Ca distribution coincides well with the Y and P distributions. Suzuki and Yogo (1986), however, found that transparent portions of young zircon grains contain no detectable amount of Ca irrespective of the high concentration of Y_2O_3 (up to 3.8 wt.%) and P_2O_5 (up to 1.8 wt.%). The Ca enrichment, therefore, appears to be secondary and to have occurred only in domains enriched in the xenotime component. The xenotime-rich zones or portions of zircon are easily degraded into a metamict state. Because xenotime has greater concentrations of U and Th than coexisting zircon (Suzuki et al., 1992), the positive correlation of Ca and U (+Th) is possible in extensively metamict zircon. The PbO contents, as high as 350 ppm, are largely correlated with the Th and U contents. But in detail, the Pb content deviates from what is expected from the decay of coexisting U and Th. For example, significant depletion in Pb can be seen at the top-right of the inner dark (Ca-rich) zone,

and unaccountable enrichment occurs at the lower end of the outer dark (Ca-rich) zone. Actually the high Ca (>0.05 wt.%) domains yield apparent ages from 212 to 814 Ma, while the low Ca domains yield 398–631 Ma apparent ages with an average of 516 Ma. We conclude that the Ca and S contents can be used independently from U–Th–Pb data as chemical criteria to discriminate between altered domains and less-altered domains where the closed system behavior of the Th–U–Pb system is maintained.

4.4. Age mapping

The age-mapping technique highlights the geometry and distribution of age domains at a micrometer scale within a single grain (Williams et al., 1999). Most age-mapping techniques are applied to Proterozoic or older monazite that contains sufficient amounts of Pb (>2000 ppm) and show differences in age on the order of 100 Ma or more (Goncalves et al., 2005). Age mapping of young monazite and zircon is equally important to place age results into petrologic and structural context with the tectonic history.

From the intrinsic response of the JCXA-733 detector, a dwell time of 0.5 to 1 s may be sufficient for monazites with 1.0 wt.% PbO under a 15 keV and 150 nA condition. However, the dwell time required for young monazites with 300–600 ppm PbO ranges from 50 to 100 s to obtain a statistically significant number of counts. Further, for age mapping of young monazite, we cannot apply a single background value determined previously, because background intensity is strongly influenced by composition. The background maps for individual spectrometers are indispensable. The time required to make a map with 200 × 200 pixels, for example, is unrealistic. Alternatively, we use 3 spectrometers for the Pb measurement with a beam current
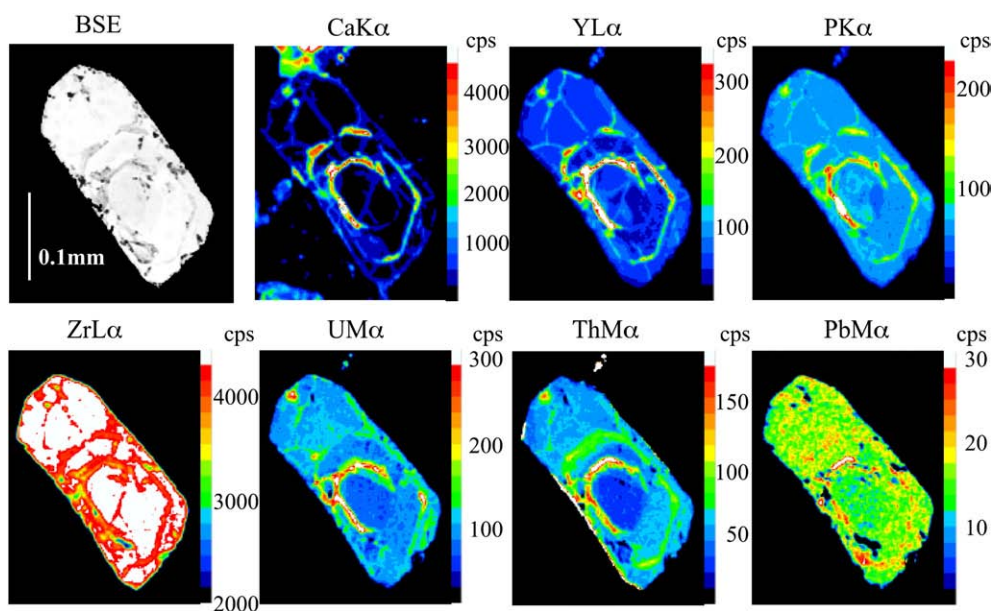

Fig. 13. BSE image and X-ray intensity of maps of zircon in sample of hornblende–biotite granite from Madagascar. Analytical conditions for this mapping were 15 keV, 300 nA and 3 s dwell time for the Ca, Y, P and Zr measurement and 700 nA and 5 s dwell time for the Th, U, Pb and background measurement, and pixel step = 2 μm.
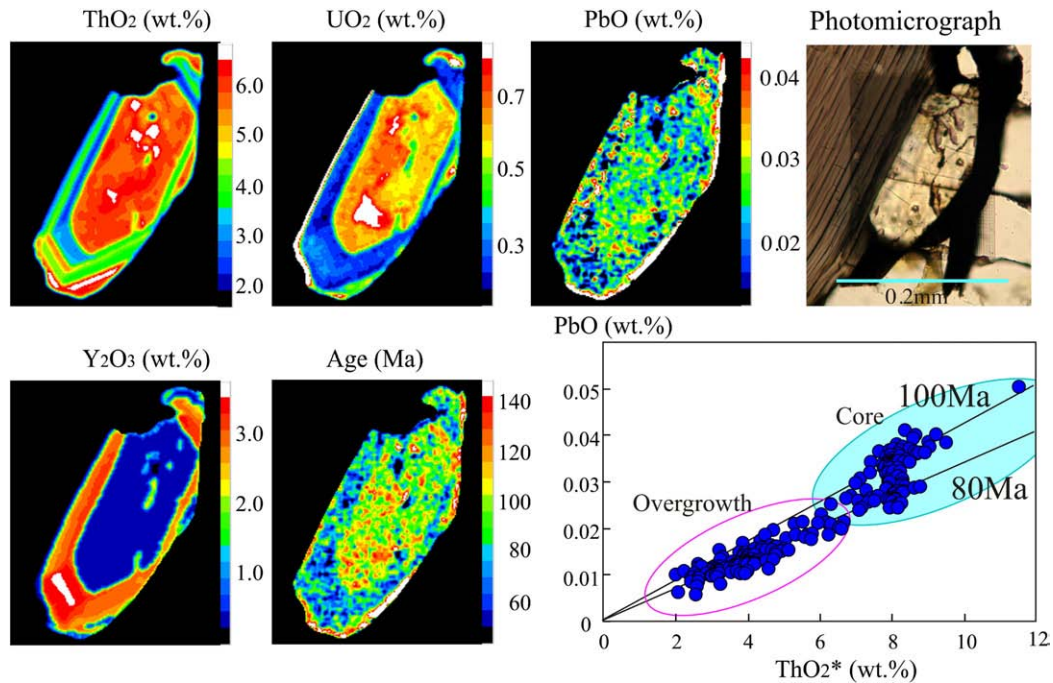
Fig. 14. Photomicrograph (plane polarized light), compositional maps, a chronological map, and a PbO–ThO$_2$* plot for a monazite grain in sillimanite–orthoclase migmatite from the Ryoke metamorphic belt of the Aoyama area, Mie Prefecture, Japan (modified from Suzuki, 2006).

as high as 1000 nA. The other spectrometer is used for acquiring a background map from which background maps for individual line positions of every spectrometer are calculated through the intensity relationships determined in advance of the measurement. Normally, the ThMα, UMβ and YLγ intensities are measured prior to the PbMα and background acquisitions with a probe current of 200 to 500 nA. By using two spectrometers for UMβ measurement, we adopt a dwell time of 1 s for the measurement of ThMα, UMβ and YLγ. We further shorten the measurement time by skipping the area outside the desired mineral. Usually, the time needed for 200 × 200 pixels mapping of c. 100 Ma monazite is shorter than 30 h. Age mapping of old monazite can be done within 10–15 h.

The raw intensity data are first corrected for background and interference and converted into concentration in the same way as the spot by spot analysis. Apparent ages of individual spots are calculated by assuming no initial Pb by Eq (5). These calculations are handled on NEC PC-98 using the N88-BASIC(86) programming environment. Translation of calculating programs for the FreeBSD environment is in progress. Compositional and age maps are constructed using an "EPMACOLORMAP" (Kato, unpublished) program on the Windows environment.

An example of age map of young monazite in migmatite sample from the Cretaceous Ryoke metamorphic belt, central Japan is given in Fig. 14, together with the Th, U, Pb and Y compositional maps. The analytical conditions used for mapping are 15 keV, 1000 nA for PbMα and background and 210 nA for others, time per pixel = 5 s for PbMα and background and 3 s for others, and pixel step = 2 μm. The Ryoke belt is a typical high temperature/pressure metamorphic belt developed in southwestern Japan as one of the circum-Pacific orogenic belts. It is composed mainly of metasedimentary rocks representing the

andalusite–sillimanite grade metamorphism and a variety of syn- to post-tectonic granitoids. The monazite ages for the gneiss concentrate between 102 and 98 Ma and are interpreted as the timing of monazite formation under lower amphibolite facies conditions, and granitic intrusion lasted from c. 95 Ma to c. 68 Ma at intervals of 2–10 Ma with a peak of plutonism at 85–80 Ma (Suzuki and Adachi, 1998). The migmatite is well-foliated and shows a mineral assemblage of sillimanite, cordierite, biotite, microcline-microperthite and sodic oligoclase with a trace amount of secondary muscovite. Accessory minerals include monazite, zircon, apatite and ilmenite, but no tourmaline can be seen. Most monazite grains form euhedral short prisms of 0.1–0.2 mm in length (see photomicrograph in Fig. 14). Some grains show the core–overgrowth relationship with a euhedral core, suggesting two-stage growth of monazite under melt-predominated conditions.

The X-ray maps discriminate between the euhedral core and overgrowth. The core, showing a rather homogeneous composition, is characterized by high concentrations of Th and U and by low concentration of Y. The euhedral overgrowth, on the other hand, shows high concentration of Y and low concentrations of Th and U. The development of oscillatory and sector zoning reinforces that the euhedral mantle formed during anatexis. The calculated age map shows the simple core–overgrowth structure that is consistent with the X-ray maps. The ages range from 70 to 130 Ma for the core, and from 50 to 110 Ma for the overgrowth in the mapping analysis. Data points obtained through spot by spot analysis on the core domain fall in the region of 100 and 80 Ma reference isochrons, whereas those on the overgrowth cluster along the 80 Ma reference isochron. The age mapping of monazite is applicable to unravel metamorphic and tectonic history of young orogenic belts as well as old ones.

Digital mapping of low Pb minerals requires measurement of line peak and background intensities of at least three constituents, Th, U, and Pb, at extraordinarily high probe current, which sometimes causes severe damage on mineral surface and carbon coating at and around metamict portions, cleavages, and cracks. This damage, which is shown in photomicrograph in Fig. 14, makes the surface of the grain unsuitable for precise determination of the Th, U, and Pb contents. We therefore prefer spot analyses coupled with examination of polished thin sections under the optical microscope before the digital mapping for assessing chronological heterogeneity. Nonetheless, we realize that spot analyses give only an approximate definition of age domains suitable only for reconnaissance. We normally carry out digital mapping, if necessary, after the spot analysis.

5. Concluding remarks

This paper describes the procedure of CHIME dating and age mapping implemented at the Center for Chronological Research, Nagoya University, together with pitfalls for quantitative analyses of trace elements with EPMA. We assessed the roles of collimator slit, detector gas, accelerating voltage, probe current, X-ray interferences and count rate in affecting the uncertainty. Many of the problems cited in the text are reduced or minimized by flexible adjustment of parameters. This paper described a way to access the Th and U interference corrections without pure Th- and U-oxides or synthesized pure $ThSiO_4$. The important assumption for EPMA chemical dating is the closed system behavior in the Th–U–Pb system. Chemical criteria, the $(Ca+Si)/(Th+U+Pb+S)$ ratio for monazite and the Ca and S concentrations for zircon, can successfully discriminate possibly concordant age data from discordant ones.

Geological histories involve multiple episodes of mineral growth, and the complexities are recorded in polygenetic Th- and U-bearing accessory minerals including monazite, xenotime, zircon and polycrase. Dating of micron-sized domains of these minerals provides a new vista for deciphering the geologic histories, but micron-sized domains are hard to analyze with the conventional mass-spectroscopic techniques. A powerful approach with a secondary ion mass spectrometer (e.g. SHRIMP; Compston et al., 1984) is restricted to limited number of laboratories. Further, the spatial resolution of secondary ion mass spectrometer (c. 20 μm) is not sufficient compared with the size of age domains in the accessory minerals. EPMA dating is an alternative way to approach "microgeochronology", and offers high spatial resolution (1–3 μm). Although EPMA dating does not provide direct information about discordance in the Th–U–Pb system, chemical criteria can discriminate possibly concordant age data from discordant ones. The regression-based CHIME technique has the advantage of substantial precision and the ability to work with minerals that contain certain amounts of initial Pb. The CHIME dating gives reliable age information and is a powerful adjunct to isotopic dating. It is well-suited to the study of metamorphic and igneous rocks where mineral grains show age zoning, as well as sedimentary rocks where mineral grains are not chronologically homogeneous and large amounts of age data are required to characterize a population.

Rigorous evaluation of the accuracy of EPMA age determination requires composition as well as age standards of monazite, xenotime, zircon and polycrase. Identifying compositionally homogeneous mineral grains and performing wet chemical analyses in these potential analytical standards are the next step towards improving the EPMA dating technique.

Acknowledgements

References

Åmli, R., Griffin, W., 1975. Microprobe analysis of REE minerals using empirical correction factors. American Mineralogist 60, 599–606.

Andreoli, M.A., Smith, C.B., Watkeys, M., Moore, J.M., Ashwal, L.D., Hart, R.J., 1994. The geology of the Steenkampskraal monazite deposit, South Africa: implications for REE–Th–Cu mineralization in charnockite-granulite terranes. Economic Geology 89, 994–1016.

Asami, M., Suzuki, K., Grew, E.S., 2002. Chemical Th–U–total Pb dating by electron microprobe analysis of monazite, xenotime and zircon from the Archean Napier Complex, East Antarctica: evidence for ultra-high-temperature metamorphism at 2400 Ma. Precambrian Research 114, 249–275.

Asami, M., Suzuki, K., Grew, E.S., 2005. Monazite and zircon dating by the chemical Th–U–total Pb isochron method (CHIME) from Alasheyev Bight to the Sør Rondane Mountains, East Antarctica: a reconnaissance study of the Mozambique suture in Eastern Queen Maud Land. Journal of Geology 113, 59–82.

Bence, A.E., Albee, A.L., 1968. Empirical correction factors for the electron microanalysis of silicates and oxides. Journal of Geology 76, 382–403.

Biju-Sekhar, S., Yokoyama, K., Pandit, M.K., Okudaira, T., Yoshida, M., Santosh, M., 2003. Late Paleoproterozoic magmatism in Delhi Fold Belt, NW India and its implication: evidence from EPMA chemical ages of zircons. Journal of Asian Earth Sciences 22, 189–207.

Bowles, J.F.W., 1990. Age dating of individual grains of uraninite in rocks from electron microprobe analyses. Chemical Geology 83, 47–53.

Burger, A.J., Von Knorring, O., Clifford, T.N., 1965. Mineralogical and radiometric studies of monazite and sphene occurrences in the Namib Desert, South-West Africa. Mineralogical Magazine 35, 519–528.

Cameron-Schimann, M., 1978. Electron microprobe study of uranium minerals and its application to some Canadian deposits. PhD thesis, the University of Alberta.

Chakhouradian, A.R., Mitchell, R.M., 1998. Lueshite, pyrochlore and monazite-(Ce) from apatite–dolomite carbonatite, LesnayaVaraka complex, Kola Peninsula, Russia. Mineralogical Magazine 62, 769–782.

Cocherie, A., Albarede, F., 2000. An improved U–Th–Pb age calculation for electron microprobe dating of monazite. Geochimica et Cosmochimica Acta 65, 4509–4522.

Cocherie, A., Legendre, O., Peucat, L.L., Kouamelan, A.N., 1998. Geochronology of polygenetic monazites constrained by in situ electron microprobe Th–U–total lead determination: Implications for lead behavior in monazite. Geochimica et Cosmochimca Acta 62, 2475–2497.

Compston, W., Williams, I.S., Meyer, C., 1984. U–Pb geochronology of zircons from lunar breccia 73217 using a sensitive high mass-resolution ion microprobe. Journal of Geophysical Research 89, B525–B534 Supplement.

Corfu, F., 1988. Differential response of U–Pb systems in coexisting accessory minerals, Winnipeg River Subprovince, Canadian Shield: implications for

Archean crustal growth and stabilization. Contributions to Mineralogy and Petrology 98, 312–325.

Cressey, G., Wall, F., Cressey, B.A., 1999. Differential REE uptake by sector growth of monazite. Mineralogical Magazine 63, 813–828.

Deliens, M., Piret, P., 1977. La kusuite, $(Ce^{3+},Pb^{2+},Pb^{4+})VO_4$, nouveau mineral. Bulletin de la Société Française de Minéralogie 100, 39–41.

Drake, M.J., Weill, D.F., 1972. New rare earth element standards for electron microprobe analysis. Chemical Geology 10, 179–181.

Dunkley, D.J., Suzuki, K., Hokada, T., Kusiak, M.A., 2008. Contrasting ages between isotopic chronometers in granulites: monazite dating and metamorphism in the Higo Complex, Japan. Gondwana Research 14, 624–643 (this issue).

Dunn, P.J., 1985. The lead silicates from Franklin, New Jersey: occurrence and composition. Mineralogical Magazine 49, 721–727.

French, J.E., Heaman, L.M., Chacko, T., 2002. Feasibility of chemical U–Th–total Pb baddeleyite dating by electron microprobe. Chemical Geology 188, 85–104.

Geisler, T., Schleicher, H., 2000. Improved U–Th–total Pb dating of zircons by electron microprobe using a simple new background modeling procedure and Ca as a chemical criterion of fluid-induced U–Th–Pb discordance in zircon. Chemical Geology 163, 269–285.

Geller, J.D., Herrington, C., 2002. High count rate electron probe microanalysis. Journal of Research of the National Institute of Standards and Technology 107, 503–508.

Goncalves, P., Williams, M.L., Jercinovic, M.J., 2005. Electron-microprobe age mapping of monazite. American Mineralogist 90, 578–585.

Grauert, B., Hänny, R., Soptrajanova, G., 1974. Geochronology of poly-metamorphic and anatectic gneiss region: the Moldanubicum of the area Lam-Deggendorf, Eastern Bavaria, Germany. Contributions to Mineralogy and Petrology 45, 37–63.

Hawkins, D.P., Bowring, S.A., 1997. U–Pb systematics of monazite and xenotime: case studies from the Paleoproterozoic of the Grand Canyou, Arizona. Contributions to Mineralogy and Petrology 127, 87–103.

Hokada, T., Misawa, K., Yokoyama, K., Shiraishi, K., Yamaguchi, A., 2004. SHRIMP and electron microprobe chronology of UHT metamorphism in the Napier Complex, East Antarctica: implications for zircon growth at >1000 °C. Contributions to Mineralogy and Petrology 147, 1–20.

Jercinovic, M.J., Williams, M.L., 2005. Analytical perils (and progress) in electron microprobe trace element analysis applied to geochronology: back-ground acquisition, interferences, and beam irradiation effects. American Mineralogist 90, 526–546.

Johann, H.H., 1931. Die Erzeugung lichstarker Röntogenspektren mit Hilfe von Konkavkristallen. Zeitschrift für Physik 69, 185–206.

Kato, T., 2005. New accurate Bence–Albee α-factors for oxides and silicates calculated from the PAP correction procedure. Geostandards and Geoanalytical Research 29, 83–94.

Kato, T., 2007. Monte Carlo study of quantitative electron probe microanalysis of monazite with a coating film: comparison of 25 nm carbon and 10 nm gold at $E_0 = 15$ and 25 keV. Geostandards and Geoanalytical Research 31, 89–94.

Kato, T., Suzuki, K., Adachi, M., 1999. Computer program for the CHIME age calculation. The Journal of Earth and Planetary Sciences, vol. 46. Nagoya University, pp. 49–56.

Kato, T., Cho, D.L., Suzuki, K., 2005. Determination of interference correction factors and preparation of standard materials using "working standard" technique for CHIME dating. Bulletin of the Nagoya University Museum 21, 43–49 (in Japanese with English abstract).

Köppel, V., 1974. Isotopic U–Pb ages of monazites and zircons from the crust–mantle transition and adjacent units of the Iveria and Ceneri zones (Southern Alps, Italy). Contributions to Mineralogy and Petrology 43, 55–70.

Köppel, V., Grünenfelder, M., 1971. A study of inherited and newly formed zircons from paragneisses and granitised sediments of the Strona-Ceneri-Zone (Southern Alps). Schweizerische Mineralogische und Petrographische Mitteilungen 51, 385–409.

Kusiak, M.A., Suzuki, K., Dunkley, D.J., Lekki, J., Bakun-Czubarow, N., Paszkowski, M., Budzyń, B., 2008. EPMA and PIXE dating of monazite in granulites from Gierałtów, NE Bohemian Massif, Poland. Gondwana Research 14, 675–685 (this issue).

Lumpkin, G.R., Chakoumakos, B.C., 1988. Chemistry and radiation effects of thorite-group minerals from the Harding pegmatite, Taos County, New Mexico. American Mineralogist 73, 1405–1419.

Montel, J.M., Foret, S., Veschambre, M., Nicollet, C., Provost, A., 1996. Electron microprobe dating of monazite. Chemical Geology 131, 37–53.

Nishiya, T., Watanabe, T., Yokoyama, K., Kuramoto, Y., 2003. New isotopic constraints on the age of the Halls Reward Metamorphics, North Queenland, Australia: Delamerian metamorphic ages and Grenvil detrital zircons. Gondwana Research 6, 241–249.

Osada, Y., 2005. Monte Carlo study of quantitative EPMA analysis of a non-conducting sample with a coating film. X-ray Spectrometry 34, 96–100.

Parrish, R.R., 1990. U–Pb dating of monazite and its application to geological problems. Canadian Journal of Earth Sciences 27, 1431–1450.

Parslow, G.R., Brandstatter, F., Kurat, G., Thomas, D.J., 1985. Chemical ages and mobility of U and Th in anatectites of the Cree Lake zone, Saskatchewan. Canadian Mineralogist 23, 543–552.

Pyle, J.M., Spear, F.S., Wark, D.A., Daniel, C.G., Storm, L.C., 2005a. Contributions to precision and accuracy of monazite microprobe ages. American Mineralogist 90, 547–577.

Pyle, J.M., Spear, F.S., Cheney, J.T., Layne, G., 2005b. Monazite ages in the Chesham Pond Nappe, SW New Hampshire: implications for assembly of central New England thrust sheets. American Mineralogist 90, 592–606.

Rhede, D., Wendt, I., Förster, H.J., 1996. A three-dimensional method for calculating independent chemical U/Pb-and Th/Pb-ages of accessory minerals. Chemical Geology 130, 247–253.

Santosh, M., Yokoyama, K., Biju-Sekhar, S., Rogers, J.J.W., 2003. Multiple tectonothermal events in the grranulite blocks of southern India revealed from EPMA dating: implications on the history of supercontinents. Gondwana Research 6, 29–63.

Santosh, M., Yokoyama, K., Acharyya, S.K., 2004. Geochronology and tectonic evolution of Karimnagar and Bhopalpatnam granulite belts, central India. Gondwana Research 7, 501–518.

Santosh, M., Tanaka, K., Yokoyama, K., Collins, A.S., 2005. Late Neoproter-ozoic–Cambrian felsic magmatism along transcrustal shear zones in southern India: U–Pb electron microprobe ages and implications for the amalgamation of the Gondwana Supercontinent. Gondwana Research 8, 31–42.

Santosh, M., Morimoto, T., Tsutsumi, Y., 2006a. Geochronology of the khondalite belt of Trivandrum Block, Southern India: electron probe ages and implications for Gondwana tectonics. Gondwana Research 9, 261–278.

Santosh, M., Collins, A.S., Tamashiro, I., Koshimoto, S., Tsutsumi, Y., Yokoyama, K., 2006b. The timing of ultrahigh-temperature metamorphism in Southern India: U–Th–Pb electron microprobe ages from zircon and monazite in sapphirine-bearing granulites. Gondwana Research 10, 128–155.

Santosh, M., Sajeev, K., Li, J.H., 2006c. Extreme crustal metamorphism during Columbia supercontinent assemble: evidence from North China Craton. Gondwana Research 10, 256–266.

Santosh, M., Tsunogae, T., Li, J.H., Liu, S.J., 2007. Discovery of sapphirine-bearing Mg–Al granulites in the North China Craton: implications for Paleoproterozoic ultrahigh temperature metamorphism. Gondwana Research, 11, 263–285.

Schärer, U., Allègre, C.J., 1982. Uranium–1ead system in fragments of a single zircon grain. Nature 295, 585–587.

Silver, L.T., Deutsch, S., 1963. Uranium–1ead isotopic variations in zircons: a case study. Journal of Geology 71, 721–758.

Smellie, J.A.T., Cogger, N., Herrington, J., 1978. Standards for quantitative microprobe determination of uranium and thorium with additional information on the chemical formulae of davidite and euxenite–polycrase. Chemical Geology 22, 1–10.

Souza, Z.S., Montel, J.M., Gioas, S.M.L.C., Hollanda, M.H.B., Nascimento, M.A.L., Sá, E.F.J., Amara, V.E., Pimentel, M.M., Lardeaux, L.M., Veschambre, M., 2006. Electron microprobe dating of monazite from high-T shear zones in the São Joée de Campestre Massif, NE Brazil. Gondwana Research 9, 441–455.

Steiger, R.H., Jäger, E., 1977. Subcommision on geochronology: convention on the use of decay constants in geo- and cosmochronology. Earth Planetary Science Letters 36, 359–362.

Suzuki, K., 1987a. Discordant distribution of U and Pb in zircon of Naegi granite: a possible indication of Rn migration through radiation damage. Geochemical Journal 21, 173–182.

Suzuki, K., 1987b. Grain-boundary enrichment of incompatible elements in some mantle peridotites. Chemical Geology 63, 319–334.

Suzuki, K., 2005. CHIME (chemical Th–U–total Pb isochron method) dating on the basis of electron microprobe analysis. Journal of Geological Society of Japan 111, 509–526 (in Japanese with English abstract).

Suzuki, K., 2006. Dating of minerals on an electron microprobe. Bunseki (Analytical Chemistry) 4, 152–159 (in Japanese).

Suzuki, K., Adachi, M., 1991a. Precambrian provenance and Silurian metamorphism of the Tsubonosawa paragneiss in the South Kitakami terrane, Northeast Japan, revealed by the chemical Th–U–total Pb isochron ages of monazite, zircon and xenotime. Geochemical Journal 25, 357–376.

Suzuki, K., Adachi, M., 1991b. The chemical Th–U–total Pb isochron ages of zircon and monazite from the gray granite of the Hida Terrane, Japan. The Journal of Earth and Planetary Sciences, vol. 38. Nagoya University, pp. 11–38.

Suzuki, K., Adachi, M., 1998. Denudation history of the high T/P Ryoke metamorphic belt, Southwest Japan: constraints from CHIME monazite ages of gneisses and granitoids. Journal of Metamorphic Geology 16, 23–37.

Suzuki, K., Yogo, S., 1986. Microprobe analyses of zircon in some granitic rocks with special reference to the distribution of uranium. Bulletin of the Nagoya University Museum 2, 27–53.

Suzuki, K., Adachi, M., Tanaka, T., 1991. Middle Precambrian provenance of Jurassic sandstone in the Mino Terrane, central Japan: Th–U–total Pb evidence from an electron microprobe monazite study. Sedimentary Geology 75, 141–147.

Suzuki, K., Adachi, M., Yamamoto, K., Nakai, Y., 1992. Intra-grain distribution of REE and crystallization sequence of accessory minerals in the Cretaceous Busetsu Granite at Okazaki, central Japan. Geochemical Journal 26, 383–394.

Suzuki, K., Dunkley, D., Adachi, M., Chwae, U., 2006. Discovery of a c. 370 Ma granitic gneiss clast from the Hwanggangri pebble-bearing phyllite in the Okcheon metamorphic belt, Korea. Gondwana Research 9, 85–94.

Tetsopgang, S., Suzuki, K., Njonfang, E., 2008. Petrology and CHIME geochronology of Pan-African high K and Sr/Y granitoids in the Nkambe area, Cameroon. Gondwana Research 14, 686–699 (this issue).

Tilton, G.R., Davis, G.L., Wetheril, G.W., Aldrich, L.T., 1957. Isotopic ages of zircon from granites and pegmatites. Transactions of American Geophysical Union 38, 360–371.

Upadhyay, D., Jahn-Awe, S., Pin, C., Paquette, J.l., Braun, I., 2006. Neoproterozoic alkaline magmatism at Sivamalai, southern India. Gondwana Research 10, 156–166.

Williams, I.S., Compston, W., Chappell, B.W., 1983. Zircon and monazite U–Pb systems and histories of I-type magmas, Berridale Batholith, Australia. Journal of Petrology 24, 76–79.

Williams, I.S., Compston, W., Black, L.P., Ireland, T.R., Foster, J.J., 1984. Unsupported radiogenic Pb in zircon: a case of anomalously high Pb–Pb, U–Pb and Th–Pb ages. Contributions to Mineralogy and Petrology 88, 322–327.

Williams, M.L., Jercinovic, M.J., Terry, M.P., 1999. Age mapping and dating of monazite on the electron microprobe: Deconvoluting multistage tectonic histories. Geology 27, 1023–1026.

Williams, M.L., Jercinovic, M.J., 2002. Microprobe monazite geochronology: putting absolute time into microstructural analysis. Journal of Structural Geology 27, 1023–1026.

York, D., 1966. Least-square fitting of a straight line. Canadian Journal of Physics 44, 1079–1088.

Kazuhiro Suzuki, Professor at the Center for Chronological Research, Nagoya University, received his BSc (1970) from Aichi University of Education, his MSc (1973) and PhD (1978) from Nagoya University, Japan. Initially employed as an assistant professor at Tokyo Gakugei University in 1977, he then moved to Nagoya University in 1979 as an assistant professor and became a professor in 1995. His research fields include geology, petrology, grain-boundary geochemistry and geochronology. He has undertaken extensive geological studies in Japan, eastern Asia, Australia and East Africa. Recently his interest has extended to the archaeological field through the application ^{14}C dating. He developed a novel dating method, CHIME (chemical Th–U–total Pb isochron method), which has high spatial resolution and can be widely used in the field of geochronology. He has published over 100 research papers, including on the CHIME technique, in referred international journals.

Takenori Kato, Assistant Professor at the Center for Chronological Research, Nagoya University, Japan, graduated BSc (1993) and MSc (1995) from Nagoya University, and PhD (2007) from Nagoya University. He was employed as an assistant professor at the Department of Earth and Planetary Sciences, Graduate School of Science, Nagoya University in 1997 and moved to the Center for Chronological Research in 2001. His research fields include petrology, geochronology, and electron–solid interaction in geological samples.